

Adapt3R: Adaptive 3D Scene Representation for Domain Transfer in Imitation Learning

Albert Wilcox^{1,2}, Mohamed Ghanem¹, Masoud Moghani³, Pierre Barroso², Benjamin Joffe^{1,2}, Animesh Garg¹
¹Georgia Institute of Technology ²Georgia Tech Research Institute ³University of Toronto

<https://pairlab.github.io/Adapt3R>

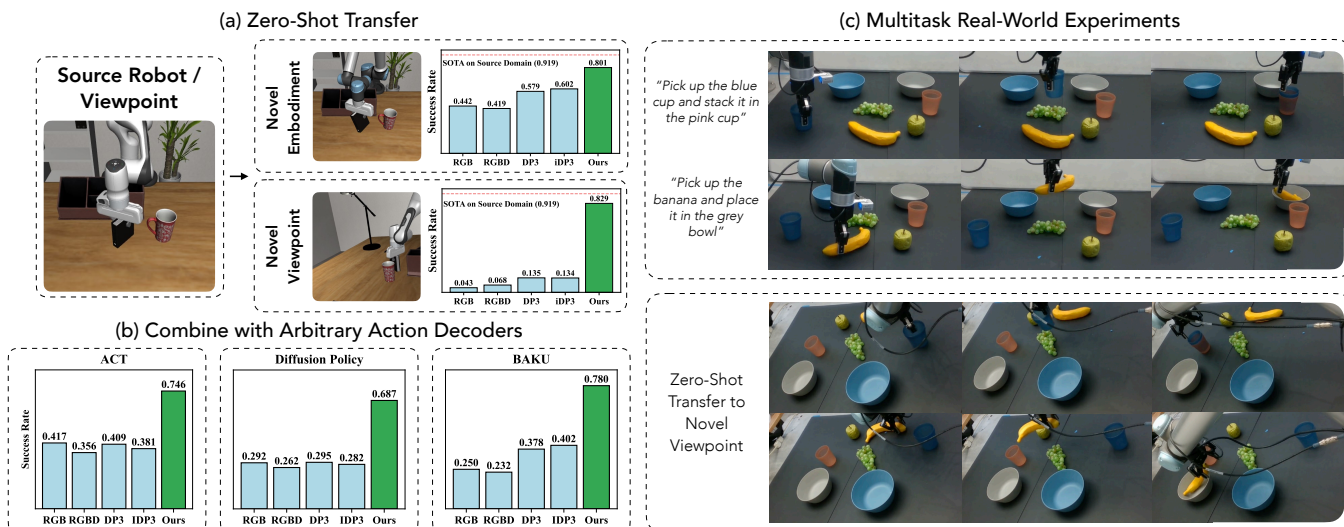


Fig. 1: Adapt3R is a unified general-purpose 3D observation encoder designed to integrate with a wide range of state-of-the-art imitation learning algorithms. (a) Adapt3R facilitates zero-shot transfer to novel embodiments and viewpoints. These plots show results when rolling out BAKU [15] with novel embodiments and viewpoints and a variety of observation encoders. (b) Adapt3R can be trained end-to-end as the encoder for a wide variety of imitation learning algorithms. This plot shows averages over all experiments in Tables II and III. (c) In a real-world multitask imitation learning benchmark, Adapt3R achieves strong performance and enables zero-shot transfer to an unseen camera pose.

Abstract—Imitation Learning (IL) has been very effective in training robots to perform complex and diverse manipulation tasks. However, its performance declines precipitously when the observations are out of the training distribution. 3D scene representations that incorporate observations from calibrated RGBD cameras have been proposed as a way to improve generalizability of IL policies, but our evaluations in cross-embodiment and novel camera pose settings found that they show only modest improvement. To address those challenges, we propose Adaptive 3D Scene Representation (Adapt3R), a general-purpose 3D observation encoder which uses a novel architecture to synthesize data from one or more RGBD cameras into a single vector that can then be used as conditioning for arbitrary IL algorithms. The key idea is to use a pretrained 2D backbone to extract semantic information about the scene, using 3D only as a medium for localizing this semantic information with respect to the end-effector. We show that when trained end-to-end with several SOTA multi-task IL algorithms, Adapt3R maintains these algorithms’ multi-task learning capacity while enabling zero-shot transfer to novel embodiments and camera poses. Furthermore, we provide a detailed suite of ablation and sensitivity experiments to elucidate the design space for point cloud observation encoders.

I. INTRODUCTION

An important goal of the robot learning community is to train generalist agents that can solve a wide variety of tasks, but this is easier said than done. Thanks to the relative ease of gathering internet-scale datasets, such models have been trained to address problems in computer vision (CV) [7, 46, 17, 37, 48, 50, 25] and natural language processing (NLP) [43, 44, 5, 1], but achieving similar success in robotics has been challenging. While recent work in multitask imitation learning has achieved impressive results when evaluated on in-distribution domains [3, 4, 51, 12, 14, 34, 15], these policies are notoriously brittle when faced with changes in factors such as camera pose, and are not able to reliably transfer to new robot embodiments.

Several large-scale data collection efforts have attempted to address this by gathering large enough datasets to sufficiently cover the state distribution [55, 56, 21], but these datasets are still orders of magnitude smaller than datasets used for CV and NLP, and are generally so diverse that it’s difficult to learn any unified representations across them. Ultimately, collecting enough data to sufficiently cover the inference distribution for

arbitrary deployment settings with brute force is likely to be prohibitively expensive, requiring a fleet of robotic hardware along with significant costs for operators and maintenance.

With all this in mind, we hypothesize that in order to train general-purpose robots, we must first design architectures that better lend themselves to generalization beyond the training dataset. There is a wide variety of work that sets out to do this, but we specifically focus on those methods that do so using 3D representations. In order to robustly complete any real-world task, a robot policy must have some 3D understanding of the world. When learning from 2D inputs alone, the robot must learn to infer this understanding, and this process is prone to overfitting to specifics of the demonstration set up, such as the camera position and the choice of robot embodiment. On the other hand, by directly training a policy on 3D representations of the world we can in theory remove this source of generalization issues.

Several lines of work have considered the application of 3D scene representations to end-to-end IL. One lifts 2D inputs from several depth cameras into rich 3D representations to be used for key pose prediction [51, 12, 13, 11, 62] but this is not easily applicable for tasks that require more dynamic motions than are possible with key pose interpolation, or settings where demonstration data comes from teleoperation data without defined key poses. Another line of work uses point clouds as inputs for diffusion policies [66, 65, 20], but these works make architectural choices which force the agent to learn to reason about the 3D geometry of the scene, which is difficult to do in low-data regimes like robotics and prone to overfitting to the training distribution. Finally, a third line of work lifts DINO [37] features into a 3D representation to achieve impressive instance generalization results [59, 58], but this method requires the hand selection of task-relevant features which is not easily scalable to multi-task setups or long-horizon tasks which may interact with several objects.

The goal of this paper is to unify these lines of work into an architecture explicitly designed for transfer to novel embodiments and camera viewpoints. To that end, we introduce Adapt3R, an Adaptive 3D Scene Representation. Adapt3R is an observation backbone that conditions on RGBD inputs from several calibrated depth cameras, and is designed to output a single representation vector that can be used as conditioning for a wide variety of IL algorithms when trained in an end-to-end setup. The key insight behind Adapt3R is to shift all of the semantic reasoning to a 2D backbone and use the 3D information specifically to localize that semantic information in the scene with respect to the end-effector. We actualize this by lifting semantic information from a pre-trained vision foundation model into a 3D point cloud and, after completing several carefully chosen alterations to the point cloud, using a learned attention pooling operation to reduce the point cloud into a single conditioning vector. Lifting the semantic features from a 2D foundation model allows us to bypass the data-intensive process of learning them directly from point clouds, and the alterations, which we discuss in detail in Section III, help the attention pooling step to reason about the points. In

summary, we contribute the following:

- The Adapt3R architecture, a novel method for extracting conditioning vectors from RGBD inputs that can be combined with a wide range of SOTA IL algorithms. Adapt3R does this by lifting semantic features into a 3D point cloud followed by a carefully designed feature extraction process.
- Experiments showing that when combined with ACT [68], Diffusion Policy [6] and BAKU [15], Adapt3R leads to strong performance on the LIBERO-90 benchmark [29], enables zero-shot generalization to novel robot embodiments, and achieves success rates an average of 56.1% higher than the next best comparison when evaluating on unseen camera poses.
- Experiments demonstrating Adapt3R’s strong performance generalizing to unseen camera viewpoints in a real-world multitask imitation learning benchmark.
- Detailed ablation studies to verify our design choices and help to elucidate the design space of point cloud encoders.

II. RELATED WORK

A. Imitation learning for robotic manipulation

Imitation learning (IL) techniques [40] learn a policy in a supervised manner from a dataset consisting of observations and paired expert demonstrator actions. Early work in this area trains policies which directly map from observations to actions [40, 67, 32, 9], but this is not well suited to realistic datasets which often contain multimodal action distributions and more complex behaviors. Several recent works have set out to address these issues using energy-based models [8], diffusion models [6, 20, 66, 62] and carefully designed transformers [68, 15, 34, 27]. While these methods achieve impressive results completing tasks within their training distributions, they still suffer when out of this distribution. Even methods which train on large scale datasets [3, 4, 36, 2, 22, 61, 60, 64, 21, 38] are brittle to changes in environment or camera pose and difficult to transfer to novel embodiments. Rather than attempting to achieve generalization purely through scaling, this paper introduces an architecture which uses 3D representations as a bridge between settings with different embodiments and camera poses.

B. 3D representations in Robot Manipulation

While the robotics community at large mostly uses 2D inputs for IL pipelines, a growing body of recent work has achieved success with 3D inputs. PerAct [51] and RVT [12, 13] use voxels and simulated camera views respectively to predict end effector keyposes, but this framework assumes tasks that can be neatly decomposed into a sequence of key frames, precluding application to tasks requiring higher-frequency control or nonlinear trajectories such as pouring or wiping. Another line of work embeds outputs of foundation models in HD scene representations [49, 63], but these require expensive inference-time training, once again precluding high-frequency control.

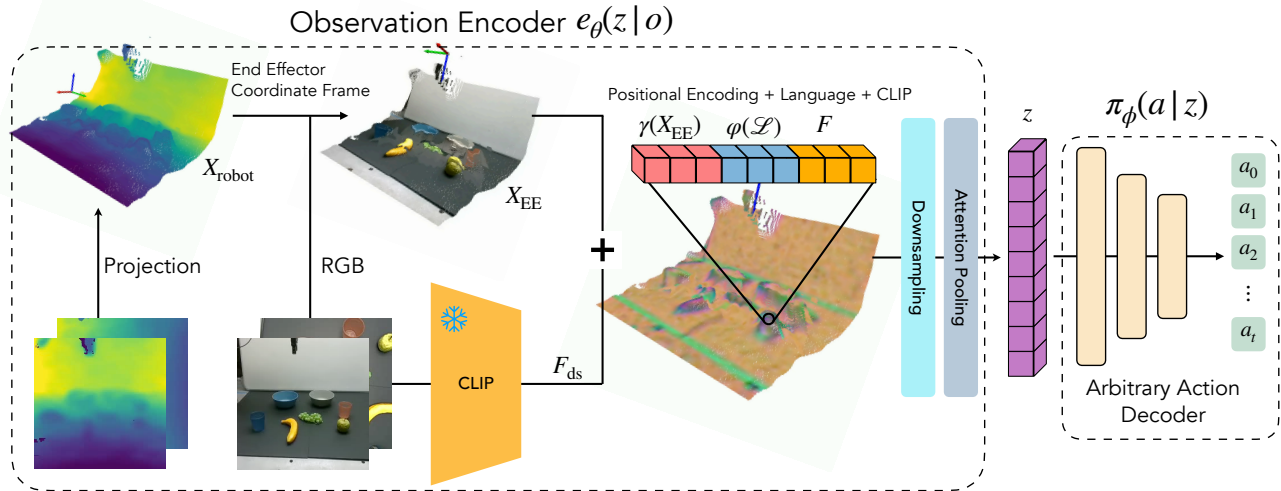


Fig. 2: Adapt3R is a unified method for extracting scene representations from RGBD inputs for imitation learning, and is designed to work well with a variety of state-of-the-art imitation learning algorithms. It starts by lifting pre-trained foundation model features on RGBD inputs into a 3D scene representation. Then, after a carefully designed point cloud processing step, it uses attention pooling to compress the point cloud into a single vector z which can be used as conditioning for a policy in an end-to-end learning setup.

Most similar to Adapt3R is a body of work which uses point clouds, a relatively cheap-to-construct scene representation, as input to a policy. Gervet et al. [11] lifts outputs from a frozen pretrained backbone (in their case CLIP [45]) into a point cloud before using this information to predict key poses, and Xian et al. [62] builds on this by learning a diffusion policy planner to connect the predicted key poses. 3D Diffuser Actor [20] uses a similar scene representation, self attends between points in the scene and cross attends between scene points, action position samples, language tokens and proprioception. In particular, self-attending between points in the scene requires the agent to reason about its 3D geometry, which is difficult to do in a low-data regime and prone to overfitting to the specifics of the training data. Adapt3R, on the other hand, is designed to use the 3D information only to localize the semantic information with respect to the end effector, enabling better transfer to novel camera viewpoints.

Another similar line of work utilizes colorless point clouds as an input modality [66, 65], followed by a PointNet [41, 42] which pools the cloud into a single vector to be used as conditioning for a diffusion policy. While this design allows generalization to novel object appearances in a single-task setup, its omission of the rich semantic information available to RGB sensors causes it to suffer in multitask setups, and its reliance on the 3D scene information once again makes it suffer when evaluated on out-of-distribution camera poses and robot embodiments. Unlike DP3, Adapt3R uses semantic information from a frozen pre-trained 2D vision backbone to enable multitask IL and alleviate the over-reliance on learning 3D geometric information from scratch.

A final line of work similar to Adapt3R uses DINO [37]

features lifted into a 3D representation to achieve impressive instance generalization results [59, 58]. The key idea behind these works is to use cosine similarity between the features in the image and a set of hand-selected reference features to infer a descriptor map of task-relevant points. This descriptor map is then used either for task planning in Wang et al. [59] or as input to a PointNet-like backbone in Wang et al. [58]. The key limitation of this work is its dependence on the hand-selected per-task features, which limits its scalability to multitask setups or long-horizon tasks with several relevant objects. Adapt3R alleviates this through the attention operation described in Section III-C, which automatically learns these features during end-to-end policy learning.

A more detailed comparison to related works is available in the supplement.

III. METHOD

Unlike prior methods, which in general make architectural choices leading the policy to infer semantic information from the point cloud, the key idea behind Adapt3R is to entirely offload the extraction of semantic information to the 2D backbone, and instead use 3D information to localize the semantic information with respect to the end-effector. In order to do this, Adapt3R first lifts RGBD images into a point cloud equipped with semantic and spatial information as described in Section III-B. Next, it computes an attention map over points in the cloud in order to reduce the cloud into a single vector as described in Section III-C. Finally, Adapt3R uses that vector as conditioning information for arbitrary downstream action decoders as described in Section III-D, and the full pipeline is trained end-to-end, as shown in Figure 2.

A. Problem Setup

We assume access to a dataset $\mathcal{D} = \{\mathcal{L}_i, (o_{i,1}, a_{i,1}), \dots, (o_{i,T_i}, a_{i,T_i})\}_{i=1}^N$ consisting of N expert demonstrations with corresponding natural language instructions \mathcal{L}_i . Each observation $o_{i,t} = (\mathcal{I}, \mathcal{R}, \mathcal{P})$ is a tuple consisting of a set of RGBD images $\mathcal{I} = \{I_1, \dots, I_{n_{\text{cam}}}\}$ streaming from n_{cam} cameras, where each image $I_i \in \mathbb{R}^{H \times W \times 4}$. We assume access to a set of corresponding camera calibration matrices mapping 2D image coordinates and depth values to 3D coordinates in the robot’s base frame, and proprioceptive information $\mathcal{P} = \{R_{\text{EE}}, g\}$, where $R_{\text{EE}} \in SE(3)$ is the end effector’s pose matrix and g is gripper state. We assume the actions $a_{i,t}$ are captured from an expert demonstrator that consistently completes the task and define $A_{i,t} = \{a_{i,t}, \dots, a_{i,t+H-1}\}$ to be the length H chunk of actions starting from timestep i .

Given this setup, Adapt3R’s goal is to learn an encoder $e_\theta(z|o)$ that subsequently maximizes the success rate of a policy $\pi_\phi(A|z)$ conditioned on e_θ ’s outputs when the two are trained together end-to-end.

B. 3D Scene Representation

In this section, we describe our method for constructing a 3D scene representation with the necessary information and structure to be useful for our end goal of compressing it into a single compact conditioning vector. Similarly to [20, 11, 62, 58, 59], we use camera calibration data to lift semantic features from several viewpoints into a single unified point cloud. Specifically, using a pre-trained frozen CLIP ResNet [45], we define a function $f: \mathbb{R}^{H \times W \times 4} \rightarrow \mathbb{R}^{H/4 \times W/4 \times d}$ which maps an $H \times W$ image to a $H/4 \times W/4 \times d$ feature map by passing the RGB subset of the image through the first layer of the CLIP ResNet, outputting the intermediate feature volume, and using a learned projection to project them to dimension d . Then, for each image I_i we use the calibration information to deproject it into a point cloud and translate that point cloud into the robot base’s coordinate frame, $X_{\text{full},i} \in \mathbb{R}^{H \times W \times 3}$. This point cloud is then resized using nearest neighbors interpolation into a smaller point cloud and flatten it to arrive at a final matrix $X_{\text{robot},i} \in \mathbb{R}^{HW/16 \times 3}$. Likewise, we flatten $f(I_i)$ to create a feature volume $F_i \in \mathbb{R}^{HW/16 \times d}$. We concatenate the point clouds from each camera input to create a combined point cloud consisting of the 3D positions $x_{\text{robot}} \in \mathbb{R}^{n_{\text{cam}}HW/16 \times 3}$ and features $F \in \mathbb{R}^{n_{\text{cam}}HW/16 \times d}$. For future convenience, we define $m = n_{\text{cam}}HW/16$ to be the number of points in the cloud.

In summary, this step lifts semantic information from a frozen 2D backbone into the point cloud. Equipping the encoder with this information means it does not need to learn to infer that semantic information directly from the point cloud. This in turn decreases the likelihood that it will overfit to the properties of the point clouds in the dataset (such as those arising from the specific camera poses that were trained on).

End Effector Coordinate Frames: Prior work using point clouds as an observation modality for IL have in general not

given significant consideration to the coordinate frame used to represent the points, often defaulting to the base coordinate frame, which we’ve found to be suboptimal. Mandlekar et al. [33] purports that wrist observations are very helpful for many robotic manipulation tasks, since they are better suited for reasoning about the relative positions of the end effector and target objects. Applying the same intuition to the point cloud modality, we use proprioceptive information R_{EE} to transform the point clouds from the base frame to the end effector’s coordinate frame, giving us the new point cloud X_{EE} .

Liu et al. [30] notes that this change can lead to improved data efficiency, but we observe that it is especially helpful for cross-embodiment learning. In this setting, it is important for the agent to be able to reason about the relative position between the end effector and objects in the scene without overfitting to the specific features of the training distribution end effector. Transforming into the end effector’s coordinate frame helps to do this.

Positional Encoding: As described in [47, 35], neural networks are not well suited to fitting data with high-frequency variation. In robotics, where a small difference in relative position between the end effector and object can have a substantial effect on the outcome of a rollout, this issue is especially important. Thus, as in [35] we use sinusoidal positional encoding to lift the point positions into a higher dimensional space more conducive to deep function approximation. Specifically, we apply the following encoding function: $\gamma(x) = (\sin(2^0\pi x), \cos(2^0\pi x), \dots, \sin(2^{L-1}\pi x), \cos(2^{L-1}\pi x))$ with $L = 10$ which lifts the positions into $\hat{x} \in \mathbb{R}^{60}$. Let $\hat{X}_{\text{EE}} = \gamma(X_{\text{EE}}) \in \mathbb{R}^{m \times 60}$ denote the lifted point cloud.

C. Point Cloud Reduction

After constructing the 3D scene representation as described in Section III-B, we now discuss our method for reducing this scene representation into a single, compact vector to be used as conditioning for the downstream policy. Unlike prior methods, which compute self-attention between points or use hierarchical PointNets to extract semantic information from the relative locations of the points in the cloud, we design our architecture to reason only about the relative location between the points and the end-effector. The key steps in this process are cropping, downsampling, and the final learned reduction.

Cropping: Some prior work depends on carefully selected cropping bounds to help isolate the important objects in the scene [66, 57] while other work forgoes cropping, arguing that it is impractical to assume access to this information [65, 20]. We take a stance in the middle, noting that especially when attempting to generalize to novel camera positions some cropping can help to ignore far away OOD background points. Specifically, we crop scenes such that the entire table is visible but objects outside the table are not. Further details about cropping, including a sensitivity study, are available in the supplement.

Next, a benefit of transforming the point clouds into the end effector’s coordinate frame is that it allows us to crop out most

of the robot. Specifically, since X_{EE} has been transformed to have the property that the positive z axis points out of the end effector, we crop out all points with negative z values in X_{EE} . This helps to enable cross-embodiment transfer by cropping out a large number of points in the robotic arm, minimizing the difference between the training and test distributions.

Downsampling: When changing camera positions, one of the biggest differences is that the new position has a very different distribution of table points than the original viewpoint. Among other things, we address this through a strategic choice in downsampling algorithm. Unlike [66, 65], which performs furthest point sampling based on Cartesian coordinates, we adopt the approach of Ke et al. [20] which notes that the furthest point sampling algorithm is defined on any metric space, and sample according to ℓ_2 distance between the feature vectors in F . Empirically, we find that this samples far fewer points on the table, where the feature vectors are relatively similar to one another, and far more points on the objects in the scene, where there is more variance in the feature vectors, and provide visualizations of this difference in the supplement. Downsampling to $p < m$ points yields a new cloud consisting of the lifted positions $\hat{X}_{EE,ds} \in \mathbb{R}^{p \times 60}$ and feature vectors $F_{ds} \in \mathbb{R}^{p \times d}$.

Language Embeddings: Prior work has found FiLM [39] modulation based on language inputs in the RGB backbone to help policies reason about their tasks in multitask settings [29, 15]. Likewise, we concatenate language embeddings to the representations of the points in our point cloud. Specifically, we define an embedding function φ which maps a language input \mathcal{L} to an embedding by passing it through a frozen pre-trained language encoder (we use CLIP) and projecting it to dimension d . We define our final point cloud $P \in \mathbb{R}^{p \times (2d+60)}$ to be the concatenation of positional encodings $\hat{X}_{EE,ds}$, feature vectors F_{ds} and language embeddings $\varphi(\mathcal{L})$.

Encoding Extraction: After following the aforementioned steps to construct a point cloud with sufficient structure, we set out to reduce the point cloud into a conditioning vector without risk of overfitting to specific attributes of the training scenes. To do this, we learn an attention map over the points and use the resulting attention pooling operation to output a final vector z which we use as conditioning for the final policy. Concretely we learn key and value MLPs $K_\theta : \mathbb{R}^{2d+60} \rightarrow \mathbb{R}^{d_k}$ and $V_\theta : \mathbb{R}^{2d+60} \rightarrow \mathbb{R}^{d_e}$, and learn a fixed query $q \in \mathbb{R}^{d_k}$. The final embedding z is defined to be

$$z = \text{softmax} \left(\frac{qK_\theta(P)}{\sqrt{d_k}} \right) V_\theta(P). \quad (1)$$

We find that in settings with very large changes in camera pose, the attention map gives very little attention to out-of-distribution points, which helps with generalization to the new viewpoint. Visualizations of these attention maps are provided in the supplementary material.

D. Policy Learning

After extracting the encoding vector z , the last step is to use it to train a policy. In this work, we evaluate Adapt3R’s

compatibility with Action Chunking Transformer (ACT) [68], Diffusion Policy (DP) [6], and BAKU [15], but it can in principle be combined with any imitation learning algorithm which uses vectors as conditioning. We briefly summarize these algorithms here and explain them in more detail in the supplement. For all algorithms, $\ell_i \in \mathbb{R}^{d_e}$ is the projected output from a pre-trained frozen language encoder (CLIP), $u_{i,t} \in \mathbb{R}^{d_e}$ is the output of a learned proprioception encoding network U_θ and $z_{i,t} \sim e_\theta(z_{i,t}|o_{i,t})$ is the output of the Adapt3R encoder.

Action chunking transformer (ACT) [68] learns to predict chunks of actions by casting the learning as a conditional variational inference problem, and sampling from the likelihood distribution which is parameterized by a transformer model [54]. Specifically, it learns an encoder $q_\phi(\eta|A_{i,t}, z_{i,t}, u_{i,t})$, where η is a latent variable, and decoder $\pi_\phi(\hat{A}_{i,t}|z_{i,t}, u_{i,t}, \ell, \eta)$ and optimizes the following variational objective:

$$\begin{aligned} \mathcal{L}(\phi) = & \text{MSE}(A_{i,t}, \pi_\phi(z_{i,t}, u_{i,t}, \ell, q_\phi(A_{i,t}, z_{i,t}, u_{i,t}))) \\ & + \beta D_{\text{KL}}(q_\phi(\eta|z_{i,t}, u_{i,t}) || \mathcal{N}(0, 1)). \end{aligned} \quad (2)$$

Diffusion policy (DP) [6] samples chunks of actions through a learned reverse Langevin dynamics process from [18]. Specifically, we sample $k \sim \text{Uniform}(\{1, 2, \dots, K\})$, $\epsilon \sim \mathcal{N}(0, I)$, and minimize

$$\mathcal{L}(\phi) = \text{MSE}(\epsilon, \epsilon_\phi(A_{i,t} + \sigma_t \epsilon, t, z_{i,t}, u_{i,t}, \ell_i)) \quad (3)$$

where σ_k is a noise scale according to the noise schedule and t is the timestep in the noising MDP.

BAKU [15] passes a sequence containing task conditioning ℓ , observation encodings $z_{i,t}$, proprioception encodings $u_{i,t}$ and a learned readout token to a transformer decoder network T_ϕ [54]. It uses the last output from the transformer as input to an MLP action head π_ϕ , which outputs a Gaussian distribution over chunks of actions. The final pipeline is trained with the following NLL objective:

$$\mathcal{L}(\phi) = -\log \pi_\phi(A_{i,t} | T_\phi(\ell, z_{i,t}, u_{i,t})[-1]). \quad (4)$$

IV. SIMULATED EXPERIMENTS

In this section, we set out to answer the following questions:

- Does Adapt3R have the capacity to achieve strong success rates in a multitask learning setting?
- How does Adapt3R perform in zero-shot cross-embodiment settings compared with baseline algorithms?
- How does Adapt3R perform in zero-shot camera viewpoint change experiments compared with baseline algorithms?
- How do the various design decisions described in Section III affect Adapt3R’s performance?

A. Benchmark

LIBERO [29] is a multitask learning benchmark consisting of several task suites designed to study lifelong learning. We evaluate on LIBERO-90, which includes 90 rigid-body

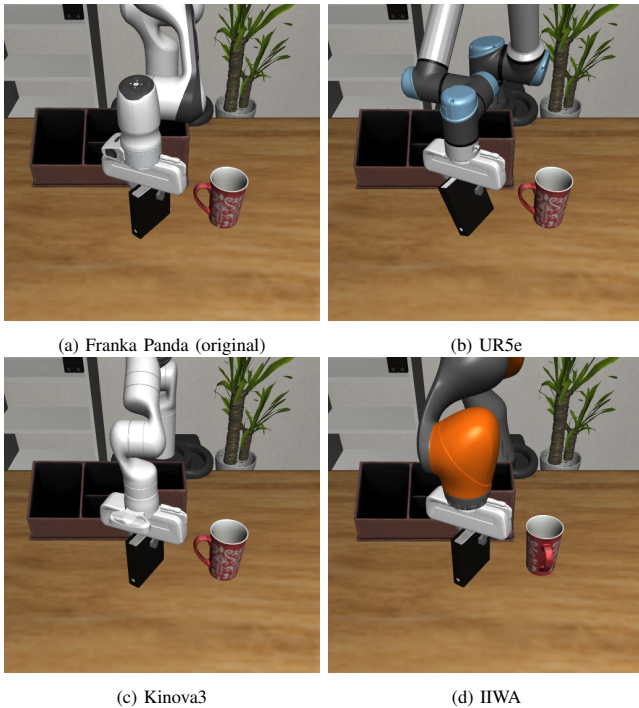


Fig. 3: We train on a dataset which only includes demonstrations using the Franka Panda (a), and evaluate zero-shot on the UR5e, Kinova3 and IIWA robots (b-d).

and articulated manipulation tasks with corresponding natural language instructions. All algorithms have access to a scene camera, wrist camera, and proprioceptive information, and there are 50 demonstrations per task, for a total of 4500 demonstrations including about 670k state-action pairs.

B. Baselines

The goal of these experiments is to understand how a variety of observation backbones affect the properties of the final learned policy. To this end, for each of the action decoders mentioned in Section III-D, our baselines run the same algorithm while replacing the observation encoder e_θ with the following backbones:

- 1) **RGB**: The CNN backbone of a ResNet-18 [16] with pre-trained ImageNet weights [7] followed by a spatial softmax [28], fine-tuned. While this comparison omits the depth information that the others have access to, we found it to be a strong baseline.
- 2) **RGBD**: Similar to RGB, but with the depth information concatenated to the RGB array along the color axis.
- 3) **DP3**: The encoder from 3D Diffusion Policy [66], which lifts the depth information into a colorless point cloud, downsamples with farthest point sampling (FPS) [41] according to position, processes points with an MLP, and aggregates them into one conditioning vector using max pooling. These point clouds have access to the same world frame cropping as Adapt3R.

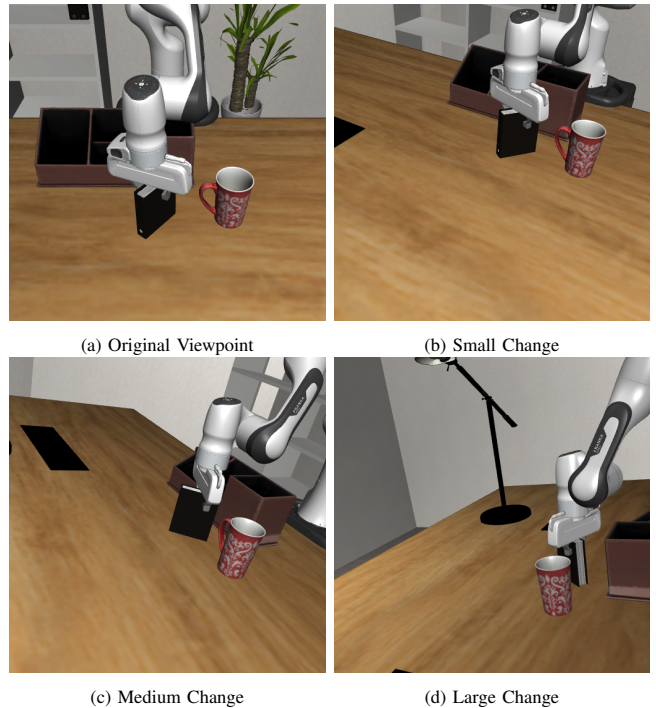


Fig. 4: During training the agent only has access to the original viewpoint (a), and we evaluate zero-shot on viewpoints with small (b), medium (c) and large (d) displacements from the original viewpoint.

- 4) **iDP3**: The Improved 3D Diffusion Policy backbone [65] is similar to DP3 in its use of colorless point clouds and FPS downsampling. It replaces the MLP point cloud extractor with a convolutional pyramid network and downsamples to a far larger number of points.

In addition to the above, we compare to 3D Diffuser Actor (3DDA) [20], which lifts a semantic feature map into the point cloud and denoises action sequences (similarly with DP) by self-attending on the set of points and cross-attending between points and noisy action sequences.

All baselines have access to the same set of camera inputs, camera calibration data, proprioceptive information and language instructions as Adapt3R. We train 5 seeds for each algorithm variation and perform 50 evaluation rollouts per environment per seed.

C. Multitask Behavior Cloning

In this experiment, we set out to understand whether Adapt3R has the modeling capacity to achieve strong success rates on par with baseline observation encoders when rolling out in an in-distribution multitask setting.

We present results for LIBERO-90 in Table I. Overall, we see that Adapt3R does in fact have the modeling capacity to achieve strong results on in-distribution settings, achieving similar performance to baselines in all experiments, and achieving the strongest overall success rate when combined with BAKU.

TABLE I: Success rates for in-distribution evaluations on the LIBERO 90 benchmark. We see that Adapt3R has a similar modeling capacity to strong baselines such as RGB and 3DDA for LIBERO 90.

| Encoder | ACT | Diffusion Policy | BAKU |
|-------------------|--------------|------------------|--------------|
| RGB | 0.908 | 0.905 | 0.914 |
| RGBD | 0.705 | 0.868 | 0.789 |
| DP3 | 0.753 | 0.687 | 0.681 |
| iDP3 | 0.758 | 0.668 | 0.758 |
| 3D Diffuser Actor | - | 0.837 | - |
| Adapt3R | 0.903 | 0.880 | 0.919 |

One takeaway is that Adapt3R has far stronger performance than DP3 and iDP3, which do not include semantic features, indicating that 3D geometry alone is not enough to succeed in multitask settings. Another surprising takeaway is that RGBD performs worse than RGB despite having access to more information. This is likely because the wrist camera helps with the spatial reasoning that depth would otherwise help with and the depth is simply extra information that is difficult for the policy to make sense of with the RGBD baseline’s relatively naïve 3D encoder.

D. Cross Embodiment

In this section, we investigate whether Adapt3R leads to improved performance in a zero-shot cross-embodiment setting. In particular, we train on the original dataset, which uses a Franka Panda robotic arm [10]. Then, we replace the robot with a variety of alternative arms, including the UR5e [53], Kinova3 [24], and Kuka IIWA [26] robots, as shown in Figure 3. Having replaced the robots, we evaluate on the full LIBERO-90 benchmark.

Results are shown in Table II. Overall, we see that Adapt3R outperforms all comparison encoders across all robots when combined with any action decoder, indicating its capability to imbue a variety of action decoders with zero-shot cross-embodiment capabilities. An interesting result is that 3DDA achieves similar performance to Adapt3R while DP3 sees a large drop in performance. A possible explanation for this is that, since it has access to semantic information from the CLIP embeddings, it is reasoning more about the objects in the scene whereas DP3, which only has access to colorless points, is inferring task progress based on points on the robot, leading to problems with the new embodiments.

E. Change of Camera Position

In this section, we investigate whether Adapt3R leads to improved performance when rolling out using an unseen camera viewpoint. In LIBERO, we train using the original viewpoints from the dataset, which include a scene camera and a wrist camera. At inference time, we perturb the scene camera by small, medium, and large perturbations, as shown in Figure 4.

Results are presented in Table III. Overall we see that Adapt3R consistently leads to a substantial boost in performance over comparison observation encoders, especially in

TABLE II: Success rates when rolling out policies in a zero-shot cross-embodiment setting. We see that Adapt3R consistently outperforms all other observation encoders and achieves similar performance to 3DDA.

| Algorithm | UR5e | Kinova3 | IIWA |
|-------------------|--------------|--------------|--------------|
| ACT + RGB | 0.578 | 0.643 | 0.525 |
| ACT + RGBD | 0.493 | 0.505 | 0.420 |
| ACT + DP3 | 0.592 | 0.574 | 0.613 |
| ACT + iDP3 | 0.549 | 0.524 | 0.573 |
| ACT + Adapt3R | 0.777 | 0.743 | 0.714 |
| DP + RGB | 0.543 | 0.562 | 0.415 |
| DP + RGBD | 0.464 | 0.441 | 0.332 |
| DP + DP3 | 0.563 | 0.404 | 0.423 |
| DP + iDP3 | 0.490 | 0.348 | 0.383 |
| 3D Diffuser Actor | 0.722 | 0.759 | 0.651 |
| DP + Adapt3R | 0.757 | 0.529 | 0.505 |
| BAKU + RGB | 0.442 | 0.458 | 0.352 |
| BAKU + RGBD | 0.419 | 0.356 | 0.310 |
| BAKU + DP3 | 0.579 | 0.468 | 0.511 |
| BAKU + iDP3 | 0.602 | 0.530 | 0.571 |
| BAKU + Adapt3R | 0.801 | 0.653 | 0.718 |

TABLE III: Success rates when rolling out policies in a zero-shot camera change setting for LIBERO-90. We see that Adapt3R consistently outperforms all comparisons and achieves success rates an average of 56.1% higher than the next best comparison.

| Algorithm | Small | Medium | Large |
|-------------------|--------------|--------------|--------------|
| ACT + RGB | 0.310 | 0.216 | 0.230 |
| ACT + RGBD | 0.323 | 0.220 | 0.175 |
| ACT + DP3 | 0.376 | 0.218 | 0.081 |
| ACT + iDP3 | 0.280 | 0.264 | 0.096 |
| ACT + Adapt3R | 0.787 | 0.706 | 0.749 |
| DP + RGB | 0.133 | 0.058 | 0.042 |
| DP + RGBD | 0.178 | 0.075 | 0.080 |
| DP + DP3 | 0.179 | 0.174 | 0.028 |
| DP + iDP3 | 0.198 | 0.257 | 0.017 |
| 3D Diffuser Actor | 0.226 | 0.208 | 0.186 |
| DP + Adapt3R | 0.740 | 0.798 | 0.791 |
| BAKU + RGB | 0.141 | 0.061 | 0.043 |
| BAKU + RGBD | 0.176 | 0.065 | 0.068 |
| BAKU + DP3 | 0.311 | 0.261 | 0.135 |
| BAKU + iDP3 | 0.288 | 0.288 | 0.134 |
| BAKU + Adapt3R | 0.847 | 0.829 | 0.829 |

the setting with a very large change in camera viewpoint, indicating that our scene representation does a good job facilitating this type of generalization.

One interesting result is that DP3, iDP3 and 3DDA, which also use calibrated depth cameras to create a point cloud that should in theory be viewpoint-agnostic, do not do well in this setting. We theorize that this is because the changes in camera position here introduce a substantial number of unseen table points and these methods, which condition more on the 3D geometry of the scene, are more brittle in the face of this change.

F. Ablation Studies

In this section, we ablate several design decisions that contribute to Adapt3R, hoping to understand how these decisions

TABLE IV: Original distribution results, cross embodiment results and camera change results for ablated versions of Adapt3R. We find that the design decisions affect in-distribution evaluation minimally, but lead to substantial improvements in generalizability.

| Variant | Orig. | UR5e | Kinova3 | IWA | Small | Medium | Large | Average |
|------------------------|--------------|--------------|--------------|--------------|--------------|--------------|--------------|--------------|
| No EECF | 0.830 | 0.693 | 0.616 | 0.612 | 0.816 | 0.793 | 0.784 | 0.735 |
| No Image Features | 0.609 | 0.487 | 0.372 | 0.435 | 0.029 | 0.019 | 0.044 | 0.285 |
| RGB Point Cloud | 0.605 | 0.482 | 0.357 | 0.425 | 0.037 | 0.021 | 0.048 | 0.282 |
| No EE Crop | 0.913 | 0.778 | 0.674 | 0.700 | 0.834 | 0.822 | 0.821 | 0.792 |
| No Lang. Features | 0.913 | 0.787 | 0.627 | 0.649 | 0.847 | 0.822 | 0.824 | 0.781 |
| No Positional Encoding | 0.843 | 0.699 | 0.613 | 0.669 | 0.580 | 0.705 | 0.709 | 0.688 |
| Position-Based FPS | 0.916 | 0.768 | 0.596 | 0.642 | 0.717 | 0.651 | 0.709 | 0.714 |
| No Attention | 0.920 | 0.827 | 0.700 | 0.695 | 0.713 | 0.641 | 0.649 | 0.735 |
| Ours | 0.919 | 0.801 | 0.653 | 0.718 | 0.847 | 0.829 | 0.829 | 0.800 |

affect its multitask modeling capacity and ability to generalize to novel settings. In addition, we experiment with backbone choice, world frame cropping choice and pooling architecture in the supplement. Table IV presents ablated versions of Adapt3R when trained together with BAKU.

No EECF removes the transformation to the end effector’s coordinate frame. Results show that the EECF transformation leads to improvements across the board as it helps the robot reason about the end effector’s position relative to objects in the scene.

No Image Features and **RGB Point Cloud** remove image features F and replace them with nothing or the original RGB values respectively. Overall we see that removing this information leads to a substantial drop in performance, especially when generalizing to new camera poses. While other work [66, 65] purports that colorless point clouds are better suited to generalization, this result indicates that the features are useful for ignoring distractor points in OOD settings.

No EE Crop does not crop out points with negative x values in the end effector’s coordinate frame. We observe that the end effector cropping leads to a modest improvement across the board.

No Lang Features does not concatenate the language embeddings $\varphi(\mathcal{L})$ to the vectors in the lifted point cloud. We see that the presence of these features leads to a modest improvement across the board.

No Positional Encoding does not lift the $x \in \mathbb{R}^3$ to $\gamma(x) \in \mathbb{R}^{60}$. We find this change to be quite important, especially when generalizing to unseen camera poses where it leads to an average 11.2% improvement.

Position-Based FPS downsamples point clouds according to Cartesian coordinates rather than feature vectors. Results show that this design choice leads to a respectable benefit across the board, improving success rates by an average of 6.6%. It is especially helpful when transferring to novel camera views, which makes sense since one of the biggest effects the feature-based FPS has is to sample less points on the table, and changing camera views dramatically changes the distribution of table points.

No Attention uses max pooling, as in Ze et al. [66], as opposed to the attention pooling described in Section III-C. Results show that the attention operation is particularly helpful when transferring to unseen camera poses, where it gives less

attention to out-of-distribution points.

V. REAL EXPERIMENTS

In this section we investigate Adapt3R’s applicability to a real-world multitask imitation learning benchmark and whether it shows the same ability to achieve strong performance outside its training domain. In particular, we evaluate its ability to generalize zero-shot to a very different camera viewpoint.

A. Experiment Setup

The benchmark includes 6 pick-and-place tasks with between 59 and 87 demonstrations per task for an average of 73 demonstrations per task. A sample of tasks are shown in Figure 1 and the full suite is shown in the supplement. We use a Universal Robots UR5 and a Robotiq 2F-85 gripper. The setup includes two Realsense D435 scene cameras and a Realsense D405 wrist camera. A diagram of the setup is shown in Figure 5a.

For this experiment we compare the Adapt3R backbone to RGB, DP3 and 3D Diffuser Actor (3DDA), which we found to be the most informative baselines in the simulated experiments. For all observation backbones we train diffusion policies with absolute end-effector pose action space. All policies are trained in a multitask fashion using CLIP-encoded language instructions to differentiate tasks. We train with data from the scene camera shown in Figure 5b and, for our zero-shot experiments, evaluate with the scene camera shown in Figure 5c.

B. Results

For our results we record *progress towards task completion* as opposed to raw success rates, where grasping the target object corresponds to $\frac{1}{3}$ progress, bringing it into some contact with the goal object corresponds to $\frac{2}{3}$ and completing the task is $\frac{3}{3}$. We train two random seeds per policy and perform 5 evaluation trials per seed for a total of 10 trials per task per algorithm.

Training Camera Viewpoint: First we evaluate policies with the original camera pose used to collect training data, and present results in Table V. We see that although 3DDA narrowly shows the strongest performance, Adapt3R’s performance is similar and both algorithms show an improvement over the RGB and DP3 baselines. We note that DP3’s

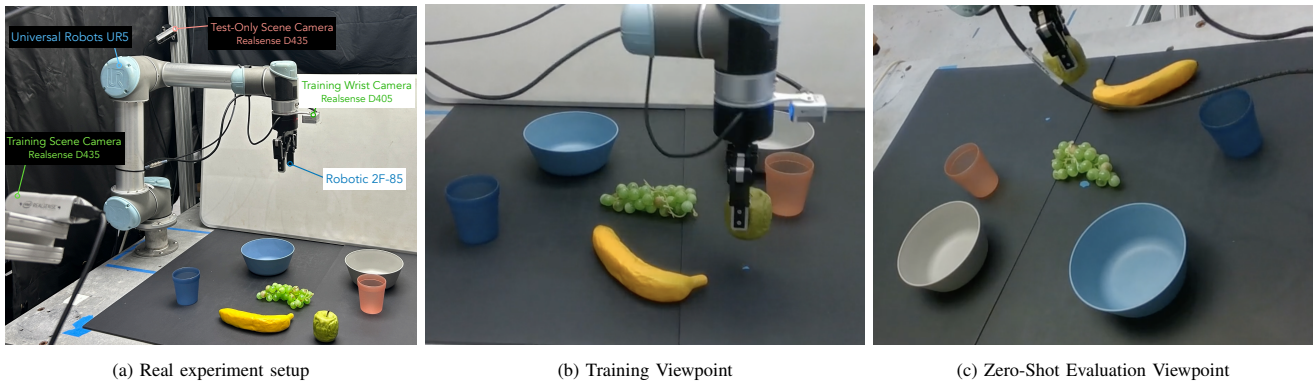


Fig. 5: (a) A diagram of our hardware setup. (b) The viewpoint used to train all policies. (c) The viewpoint used for our zero-shot evaluation experiments.

TABLE V: Average task completion for each task in our benchmark when using the original camera viewpoint.

| Algo. | Task 1 | Task 2 | Task 3 | Task 4 | Task 5 | Task 6 | Avg. |
|---------|------------|------------|-------------|-------------|-------------|------------|-------------|
| RGB | 100 | 90.0 | 43.3 | 50.0 | 50.0 | 100 | 72.2 |
| DP3 | 0.0 | 0.0 | 53.3 | 3.0 | 26.7 | 0.0 | 13.9 |
| 3DDA | 100 | 100 | 90.0 | 70.0 | 86.7 | 100 | 91.1 |
| Adapt3R | 100 | 90.0 | 93.3 | 63.3 | 80.0 | 83.3 | 85.0 |

performance was particularly poor. This was likely because, unlike 3DDA and Adapt3R which use semantic information from CLIP embeddings, it uses point locations alone to infer information about the scene, and this method performed poorly when provided with noisy outputs from the stereo depth sensor.

TABLE VI: Average task completion for each task in our benchmark when rolling out with the unseen camera viewpoint shown in Figure 5c.

| Algo. | Task 1 | Task 2 | Task 3 | Task 4 | Task 5 | Task 6 | Avg. |
|---------|------------|-------------|-------------|-------------|-------------|-------------|-------------|
| RGB | 30.0 | 16.7 | 50.0 | 0.0 | 33.3 | 36.7 | 27.8 |
| DP3 | 0.0 | 10.0 | 23.3 | 0.0 | 16.7 | 0.0 | 8.3 |
| 3DDA | 80.0 | 26.7 | 50.0 | 20.0 | 33.3 | 3.3 | 35.6 |
| Adapt3R | 100 | 83.3 | 90.0 | 53.3 | 73.3 | 76.7 | 79.4 |

Zero-shot Unseen Camera Viewpoint: Next we evaluate policies after replacing the scene camera input with the unseen camera viewpoint shown in Figure 5c, and present results in Table VI. We see that while RGB and 3DDA both achieve less than 40% of their original performance, Adapt3R’s performance drops by less than 6%. Notably, it achieves a higher average task completion out-of-distribution than RGB and DP3 do in-distribution.

As in the simulated experiments we see that although 3DDA achieves strong in-distribution performance it suffers under changes in camera pose, indicating that its architecture overfits to specifics of the scene. On the other hand, Adapt3R, whose architecture is explicitly designed to encourage the learner not to excessively condition on the relative locations of the points, does not have this issue.

VI. CONCLUSION

In this paper, we present Adaptive 3D Scene Representation (Adapt3R), a general-purpose observation encoder using 3D scene representations. The key idea behind Adapt3R is to off-load the inference of semantic information to a pretrained 2D vision foundation model, and use 3D information specifically to localize those semantic features with respect to the end-effector pose. Experimental results demonstrate that Adapt3R facilitates strong performance in multitask BC setups and leads to substantial improvements for zero-shot transfer to novel viewpoints and embodiments. Experiments in a real-world multitask IL benchmark show that Adapt3R is deployable on a physical robot and lends itself equally well to domain transfer. We hope this work can be a stepping stone towards the application of 3D representations for general autonomy.

Limitations: The most important limitation of this work is its reliance on both depth information and camera calibration matrices to facilitate the creation of fused multi-view point clouds, and the transformation to the end-effector’s coordinate frame. While this data is not difficult to collect, it is not always available in large-scale robot datasets.

REFERENCES

- [1] Josh Achiam, Steven Adler, Sandhini Agarwal, Lama Ahmad, Ilge Akkaya, Florencia Leoni Aleman, Diogo Almeida, Janko Altenschmidt, Sam Altman, Shyamal Anadkat, et al. Gpt-4 technical report. *arXiv preprint arXiv:2303.08774*, 2023.
- [2] Kevin Black, Noah Brown, Danny Driess, Adnan Esmail, Michael Equi, Chelsea Finn, Niccolo Fusai, Lachy Groom, Karol Hausman, Brian Ichter, Szymon Jakubczak, Tim Jones, Liyiming Ke, Sergey Levine, Adrian Li-Bell, Mohith Mothukuri, Suraj Nair, Karl Pertsch, Lucy Xiaoyang Shi, James Tanner, Quan Vuong, Anna Walling, Haohuan Wang, and Ury Zhilinsky. π_0 : A vision-language-action flow model for general robot control, 2024. URL <https://arxiv.org/abs/2410.24164>.
- [3] Anthony Brohan, Noah Brown, Justice Carbajal, Yevgen Chebotar, Joseph Dabis, Chelsea Finn, Keerthana

- Gopalakrishnan, Karol Hausman, Alex Herzog, Jasmine Hsu, et al. Rt-1: Robotics transformer for real-world control at scale. *arXiv preprint arXiv:2212.06817*, 2022.
- [4] Anthony Brohan, Noah Brown, Justice Carbajal, Yevgen Chebotar, Xi Chen, Krzysztof Choromanski, Tianli Ding, Danny Driess, Avinava Dubey, Chelsea Finn, et al. Rt-2: Vision-language-action models transfer web knowledge to robotic control. *arXiv preprint arXiv:2307.15818*, 2023.
- [5] Tom B Brown. Language models are few-shot learners. *arXiv preprint arXiv:2005.14165*, 2020.
- [6] Cheng Chi, Siyuan Feng, Yilun Du, Zhenjia Xu, Eric Cousineau, Benjamin Burchfiel, and Shuran Song. Diffusion policy: Visuomotor policy learning via action diffusion. *arXiv preprint arXiv:2303.04137*, 2023.
- [7] Jia Deng, Wei Dong, Richard Socher, Li-Jia Li, Kai Li, and Li Fei-Fei. Imagenet: A large-scale hierarchical image database. In *2009 IEEE conference on computer vision and pattern recognition*, pages 248–255. Ieee, 2009.
- [8] Pete Florence, Corey Lynch, Andy Zeng, Oscar A Ramirez, Ayzaan Wahid, Laura Downs, Adrian Wong, Johnny Lee, Igor Mordatch, and Jonathan Tompson. Implicit behavioral cloning. In *Conference on Robot Learning*, pages 158–168. PMLR, 2022.
- [9] Peter Florence, Lucas Manuelli, and Russ Tedrake. Self-supervised correspondence in visuomotor policy learning, 2019. URL <https://arxiv.org/abs/1909.06933>.
- [10] Franka Emika GmbH. *Panda User Manual*, 2023. Available at <https://www.franka.de>.
- [11] Theophile Gervet, Zhou Xian, Nikolaos Gkanatsios, and Katerina Fragkiadaki. Act3d: 3d feature field transformers for multi-task robotic manipulation. In *7th Annual Conference on Robot Learning*, 2023. URL <https://openreview.net/forum?id=-HFJuX1uqs>.
- [12] Ankit Goyal, Jie Xu, Yijie Guo, Valts Blukis, Yu-Wei Chao, and Dieter Fox. Rvt: Robotic view transformer for 3d object manipulation. In *Conference on Robot Learning*, pages 694–710. PMLR, 2023.
- [13] Ankit Goyal, Valts Blukis, Jie Xu, Yijie Guo, Yu-Wei Chao, and Dieter Fox. Rvt-2: Learning precise manipulation from few demonstrations. *arXiv preprint arXiv:2406.08545*, 2024.
- [14] Huy Ha, Pete Florence, and Shuran Song. Scaling up and distilling down: Language-guided robot skill acquisition. In *Proceedings of the 2023 Conference on Robot Learning*, 2023.
- [15] Siddhant Haldar, Zhuoran Peng, and Lerrel Pinto. Baku: An efficient transformer for multi-task policy learning, 2024. URL <https://arxiv.org/abs/2406.07539>.
- [16] Kaiming He, Xiangyu Zhang, Shaoqing Ren, and Jian Sun. Deep residual learning for image recognition. In *Proceedings of the IEEE conference on computer vision and pattern recognition*, pages 770–778, 2016.
- [17] Kaiming He, Xinlei Chen, Saining Xie, Yanghao Li, Piotr Dollár, and Ross Girshick. Masked autoencoders are scalable vision learners. In *Proceedings of the IEEE/CVF conference on computer vision and pattern recognition*, pages 16000–16009, 2022.
- [18] Jonathan Ho, Ajay Jain, and Pieter Abbeel. Denoising diffusion probabilistic models. *arXiv preprint arxiv:2006.11239*, 2020.
- [19] Wei Hu, Lechao Xiao, and Jeffrey Pennington. Provable benefit of orthogonal initialization in optimizing deep linear networks, 2020. URL <https://arxiv.org/abs/2001.05992>.
- [20] Tsung-Wei Ke, Nikolaos Gkanatsios, and Katerina Fragkiadaki. 3d diffuser actor: Policy diffusion with 3d scene representations. *Arxiv*, 2024.
- [21] Alexander Khazatsky, Karl Pertsch, Suraj Nair, Ashwin Balakrishna, Sudeep Dasari, Siddharth Karamcheti, Soroush Nasiriany, Mohan Kumar Srirama, Lawrence Yunliang Chen, Kirsty Ellis, et al. Droid: A large-scale in-the-wild robot manipulation dataset. *arXiv preprint arXiv:2403.12945*, 2024.
- [22] Moo Jin Kim, Karl Pertsch, Siddharth Karamcheti, Ted Xiao, Ashwin Balakrishna, Suraj Nair, Rafael Rafailov, Ethan Foster, Grace Lam, Pannag Sanketi, et al. Openvla: An open-source vision-language-action model. *arXiv preprint arXiv:2406.09246*, 2024.
- [23] Diederik P. Kingma and Jimmy Ba. Adam: A method for stochastic optimization, 2017. URL <https://arxiv.org/abs/1412.6980>.
- [24] Kinova Robotics. *Kinova Gen3 User Guide*, 2023. Available at <https://www.kinovarobotics.com>.
- [25] Alexander Kirillov, Eric Mintun, Nikhila Ravi, Hanzi Mao, Chloe Rolland, Laura Gustafson, Tete Xiao, Spencer Whitehead, Alexander C Berg, Wan-Yen Lo, et al. Segment anything. In *Proceedings of the IEEE/CVF International Conference on Computer Vision*, pages 4015–4026, 2023.
- [26] KUKA AG. *LBR iiwa Technical Data*, 2023. Available at <https://www.kuka.com>.
- [27] Seungjae Lee, Yibin Wang, Haritheja Etukuru, H Jin Kim, Nur Muhammad Mahi Shafiullah, and Lerrel Pinto. Behavior generation with latent actions. *arXiv preprint arXiv:2403.03181*, 2024.
- [28] Sergey Levine, Chelsea Finn, Trevor Darrell, and Pieter Abbeel. End-to-end training of deep visuomotor policies, 2016.
- [29] Bo Liu, Yifeng Zhu, Chongkai Gao, Yihao Feng, Qiang Liu, Yuke Zhu, and Peter Stone. Libero: Benchmarking knowledge transfer for lifelong robot learning. *Advances in Neural Information Processing Systems*, 36, 2024.
- [30] Minghua Liu, Xuanlin Li, Zhan Ling, Yangyan Li, and Hao Su. Frame mining: a free lunch for learning robotic manipulation from 3d point clouds. In *6th Annual Conference on Robot Learning*, 2022.
- [31] Ilya Loshchilov and Frank Hutter. Sgdr: Stochastic gradient descent with warm restarts, 2017. URL <https://arxiv.org/abs/1608.03983>.
- [32] Ajay Mandlekar, Danfei Xu, Roberto Martín-Martín,

- Silvio Savarese, and Li Fei-Fei. Learning to generalize across long-horizon tasks from human demonstrations, 2021. URL <https://arxiv.org/abs/2003.06085>.
- [33] Ajay Mandlekar, Danfei Xu, Josiah Wong, Soroush Nasiriany, Chen Wang, Rohun Kulkarni, Li Fei-Fei, Silvio Savarese, Yuke Zhu, and Roberto Martín-Martín. What matters in learning from offline human demonstrations for robot manipulation. *arXiv preprint arXiv:2108.03298*, 2021.
- [34] Atharva Mete, Haotian Xue, Albert Wilcox, Yongxin Chen, and Animesh Garg. Quest: Self-supervised skill abstractions for learning continuous control, 2024. URL <https://arxiv.org/abs/2407.15840>.
- [35] Ben Mildenhall, Pratul P. Srinivasan, Matthew Tancik, Jonathan T. Barron, Ravi Ramamoorthi, and Ren Ng. Nerf: Representing scenes as neural radiance fields for view synthesis. In *ECCV*, 2020.
- [36] Octo Model Team, Dibya Ghosh, Homer Walke, Karl Pertsch, Kevin Black, Oier Mees, Sudeep Dasari, Joey Hejna, Charles Xu, Jianlan Luo, Tobias Kreiman, You Liang Tan, Pannag Sanketi, Quan Vuong, Ted Xiao, Dorsa Sadigh, Chelsea Finn, and Sergey Levine. Octo: An open-source generalist robot policy. In *Proceedings of Robotics: Science and Systems*, Delft, Netherlands, 2024.
- [37] Maxime Oquab, Timothée Darcet, Théo Moutakanni, Huy Vo, Marc Szafraniec, Vasil Khalidov, Pierre Fernandez, Daniel Haziza, Francisco Massa, Alaaeldin El-Nouby, et al. Dinov2: Learning robust visual features without supervision. *arXiv preprint arXiv:2304.07193*, 2023.
- [38] Abhishek Padalkar, Acorn Pooley, Ajinkya Jain, Alex Bewley, Alex Herzog, Alex Irpan, Alexander Khazatsky, Anant Rai, Anikait Singh, Anthony Brohan, et al. Open x-embodiment: Robotic learning datasets and rt-x models. *arXiv preprint arXiv:2310.08864*, 2023.
- [39] Ethan Perez, Florian Strub, Harm De Vries, Vincent Dumoulin, and Aaron Courville. Film: Visual reasoning with a general conditioning layer. In *Proceedings of the AAAI conference on artificial intelligence*, volume 32, 2018.
- [40] Dean A Pomerleau. Alvin: An autonomous land vehicle in a neural network. *Advances in neural information processing systems*, 1, 1988.
- [41] Charles R Qi, Hao Su, Kaichun Mo, and Leonidas J Guibas. Pointnet: Deep learning on point sets for 3d classification and segmentation. *arXiv preprint arXiv:1612.00593*, 2016.
- [42] Charles R. Qi, Li Yi, Hao Su, and Leonidas J. Guibas. Pointnet++: Deep hierarchical feature learning on point sets in a metric space, 2017. URL <https://arxiv.org/abs/1706.02413>.
- [43] Alec Radford, Karthik Narasimhan, Tim Salimans, Ilya Sutskever, et al. Improving language understanding by generative pre-training. 2018.
- [44] Alec Radford, Jeff Wu, Rewon Child, David Luan, Dario Amodei, and Ilya Sutskever. Language models are unsupervised multitask learners. 2019.
- [45] Alec Radford, Jong Wook Kim, Chris Hallacy, Aditya Ramesh, Gabriel Goh, Sandhini Agarwal, Girish Sastry, Amanda Askell, Pamela Mishkin, Jack Clark, et al. Learning transferable visual models from natural language supervision. In *International conference on machine learning*, pages 8748–8763. PMLR, 2021.
- [46] Alec Radford, Jong Wook Kim, Chris Hallacy, Aditya Ramesh, Gabriel Goh, Sandhini Agarwal, Girish Sastry, Amanda Askell, Pamela Mishkin, Jack Clark, et al. Learning transferable visual models from natural language supervision. In *International conference on machine learning*, pages 8748–8763. PMLR, 2021.
- [47] Nasim Rahaman, Aristide Baratin, Devansh Arpit, Felix Draxler, Min Lin, Fred Hamprecht, Yoshua Bengio, and Aaron Courville. On the spectral bias of neural networks. In Kamalika Chaudhuri and Ruslan Salakhutdinov, editors, *Proceedings of the 36th International Conference on Machine Learning*, volume 97 of *Proceedings of Machine Learning Research*, pages 5301–5310. PMLR, 09–15 Jun 2019. URL <https://proceedings.mlr.press/v97/rahaman19a.html>.
- [48] Aditya Ramesh, Mikhail Pavlov, Gabriel Goh, Scott Gray, Chelsea Voss, Alec Radford, Mark Chen, and Ilya Sutskever. Zero-shot text-to-image generation. In *International conference on machine learning*, pages 8821–8831. Pmlr, 2021.
- [49] Adam Rashid, Satvik Sharma, Chung Min Kim, Justin Kerr, Lawrence Yunliang Chen, Angjoo Kanazawa, and Ken Goldberg. Language embedded radiance fields for zero-shot task-oriented grasping. In *7th Annual Conference on Robot Learning*, 2023. URL <https://openreview.net/forum?id=k-Fg8JDQmc>.
- [50] Robin Rombach, Andreas Blattmann, Dominik Lorenz, Patrick Esser, and Björn Ommer. High-resolution image synthesis with latent diffusion models. In *Proceedings of the IEEE/CVF conference on computer vision and pattern recognition*, pages 10684–10695, 2022.
- [51] Mohit Shridhar, Lucas Manuelli, and Dieter Fox. Perceiver-actor: A multi-task transformer for robotic manipulation. In *Proceedings of the 6th Conference on Robot Learning (CoRL)*, 2022.
- [52] Jiaming Song, Chenlin Meng, and Stefano Ermon. Denoising diffusion implicit models. In *International Conference on Learning Representations*, 2021. URL <https://openreview.net/forum?id=St1giarCHLP>.
- [53] Universal Robots A/S. *UR5e Robot User Manual*, 2023. Available at <https://www.universal-robots.com>.
- [54] Ashish Vaswani, Noam Shazeer, Niki Parmar, Jakob Uszkoreit, Llion Jones, Aidan N Gomez, Łukasz Kaiser, and Illia Polosukhin. Attention is all you need. *Advances in neural information processing systems*, 30, 2017.
- [55] Quan Vuong, Sergey Levine, Homer Rich Walke, Karl Pertsch, Anikait Singh, Ria Doshi, Charles Xu, Jianlan Luo, Liam Tan, Dhruv Shah, et al. Open x-embodiment: Robotic learning datasets and rt-x models. In *Towards*

- Generalist Robots: Learning Paradigms for Scalable Skill Acquisition@ CoRL2023*, 2023.
- [56] Homer Rich Walke, Kevin Black, Tony Z Zhao, Quan Vuong, Chongyi Zheng, Philippe Hansen-Estruch, Andre Wang He, Vivek Myers, Moo Jin Kim, Max Du, et al. Bridgedata v2: A dataset for robot learning at scale. In *Conference on Robot Learning*. PMLR, 2023.
- [57] Yixuan Wang, Zhuoran Li, Mingtong Zhang, Katherine Driggs-Campbell, Jiajun Wu, Li Fei-Fei, and Yunzhu Li. D³ fields: Dynamic 3d descriptor fields for zero-shot generalizable robotic manipulation. *arXiv preprint arXiv:2309.16118*, 2023.
- [58] Yixuan Wang, Guang Yin, Binghao Huang, Tarik Kelestemur, Jiuguang Wang, and Yunzhu Li. Gendp: 3d semantic fields for category-level generalizable diffusion policy. In *8th Annual Conference on Robot Learning*, 2024.
- [59] Yixuan Wang, Mingtong Zhang, Zhuoran Li, Tarik Kelestemur, Katherine Driggs-Campbell, Jiajun Wu, Li Fei-Fei, and Yunzhu Li. D³fields: Dynamic 3d descriptor fields for zero-shot generalizable rearrangement. In *8th Annual Conference on Robot Learning*, 2024.
- [60] Junjie Wen, Minjie Zhu, Yichen Zhu, Zhibin Tang, Jinming Li, Zhongyi Zhou, Chengmeng Li, Xiaoyu Liu, Yaxin Peng, Chaomin Shen, and Feifei Feng. Diffusion-vla: Scaling robot foundation models via unified diffusion and autoregression. *arXiv preprint arXiv:None*, 2024.
- [61] Junjie Wen, Yichen Zhu, Jinming Li, Minjie Zhu, Kun Wu, Zhiyuan Xu, Ran Cheng, Chaomin Shen, Yaxin Peng, Feifei Feng, et al. Tinyvla: Towards fast, data-efficient vision-language-action models for robotic manipulation. *arXiv preprint arXiv:2409.12514*, 2024.
- [62] Zhou Xian, Nikolaos Gkanatsios, Theophile Gervet, Tsung-Wei Ke, and Katerina Fragkiadaki. Chaineddiffuser: Unifying trajectory diffusion and keypose prediction for robotic manipulation. In *7th Annual Conference on Robot Learning*, 2023.
- [63] Justin Yu, Kush Hari, Kishore Srinivas, Karim El-Refai, Adam Rashid, Chung Min Kim, Justin Kerr, Richard Cheng, Muhammad Zubair Irshad, Ashwin Balakrishna, Thomas Kollar, and Ken Goldberg. Language-embedded gaussian splats (legs): Incrementally building room-scale representations with a mobile robot, 2024. URL <https://arxiv.org/abs/2409.18108>.
- [64] Michał Zawalski, William Chen, Karl Pertsch, Oier Mees, Chelsea Finn, and Sergey Levine. Robotic control via embodied chain-of-thought reasoning. *arXiv preprint arXiv:2407.08693*, 2024.
- [65] Yanjie Ze, Zixuan Chen, Wenhao Wang, Tianyi Chen, Xialin He, Ying Yuan, Xue Bin Peng, and Jiajun Wu. Generalizable humanoid manipulation with improved 3d diffusion policies, 2024. URL <https://arxiv.org/abs/2410.10803>.
- [66] Yanjie Ze, Gu Zhang, Kangning Zhang, Chenyuan Hu, Muhan Wang, and Huazhe Xu. 3d diffusion policy. *arXiv preprint arXiv:2403.03954*, 2024.
- [67] Tianhao Zhang, Zoe McCarthy, Owen Jow, Dennis Lee, Xi Chen, Ken Goldberg, and Pieter Abbeel. Deep imitation learning for complex manipulation tasks from virtual reality teleoperation. In *2018 IEEE international conference on robotics and automation (ICRA)*, pages 5628–5635. IEEE, 2018.
- [68] Tony Z. Zhao, Vikash Kumar, Sergey Levine, and Chelsea Finn. Learning fine-grained bimanual manipulation with low-cost hardware, 2023.
- [69] Yuke Zhu, Josiah Wong, Ajay Mandlekar, Roberto Martín-Martín, Abhishek Joshi, Soroush Nasiriany, Yifeng Zhu, and Kevin Lin. robosuite: A modular simulation framework and benchmark for robot learning. In *arXiv preprint arXiv:2009.12293*, 2020.

A. Comparison to Similar Methods

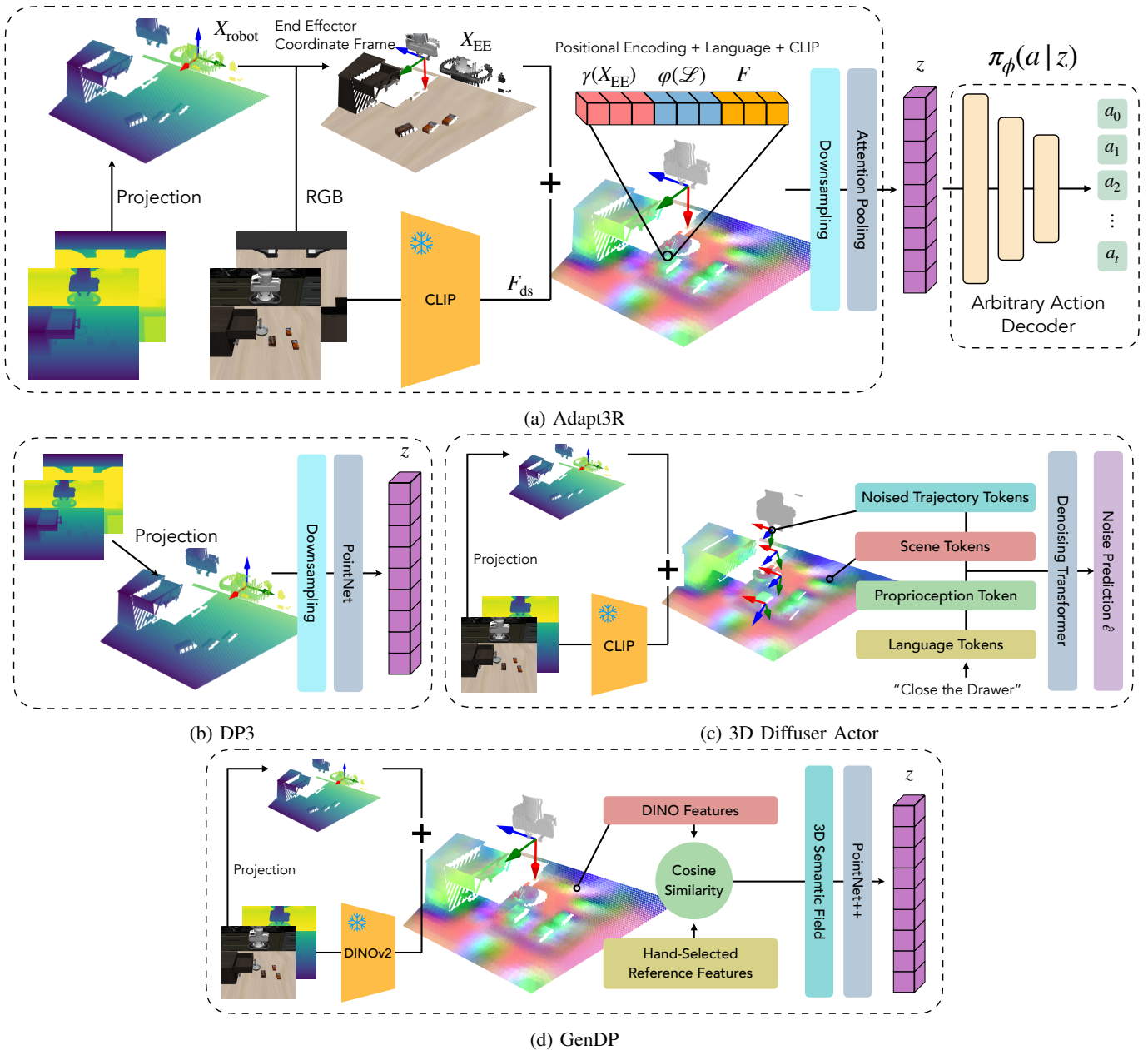


Fig. 6: In this figure we compare Adapt3R to several recent methods which also use point clouds for imitation learning. (a) We provide a diagram of Adapt3R for reference. (b) DP3 [66] omits any semantic information, instead conditioning on colorless point clouds. (c) 3D Diffuser-Actor [20] cross attends between noisy action trajectories and scene tokens. (d) GenDP [58] hand selects important reference features in the training data, and constructs semantic fields through cosine similarity between reference features and scene features.

In Figure 6 we present a comparison to several recent imitation learning algorithms which also use point clouds as a means to achieve some degree of generalization.

3D Diffusion Policy (DP3) [66] and **Improved 3D Diffusion Policy (iDP3)** [65] both operate based on the core idea that a colorless point cloud contains sufficient information to complete a variety of tasks, and show impressive results generalizing to new object instances, camera poses and scenes. They both lift the depth maps into colorless point clouds followed by cropping, some amount of downsampling and a neural network to process the points before a max pooling operation. The key difference

between the two is in their use of cropping (DP3 crops while iDP3 does not) and downsampling (DP3 downsamples much more) and their architectural choices as they are reducing over the point cloud.

As we show in our experiments in Section IV, these methods fail in multitask settings, where reasoning about semantic information regarding the items in the scene is much more important. Adapt3R differs from these methods not only in its use of semantic information from the frozen CLIP backbone, but also in its point cloud processing steps such as the positional encoding γ and the use of the feature space rather than Cartesian coordinates as the metric space for farthest point sampling.

Furthermore, as we show in Section V, these methods are particularly ill-fit to settings with noisy point cloud inputs, such as those arising from stereo depth matching. While Ze et al. [66, 65] use a LiDAR camera for their experiments, we argue that the assumption of access to high-quality point clouds is limiting, especially since some large-scale data collection efforts only provide stereo depth (eg DROID [21]). By incorporating semantic information in the point cloud, Adapt3R relies less on accurate point clouds to infer information about the scene and is able to make better sense of these noisy point clouds.

3D Diffuser Actor (3DDA) [20] is another similar method designed to use 3D scene representations to learn a diffusion policy. Specifically, it trains a transformer to, conditioned on the observation and a noisy action a_t , predict noise ϵ which can be removed from a_t to lead it closer to the original action a_0 . Note that the actions a_t are absolute pose actions.

Like Adapt3R, it lifts semantic features from a frozen CLIP model into a point cloud. It also lifts the noisy action poses into the cloud, and embeds the proprioceptive information and language instruction into more tokens. Finally, it self attends between points in the scene and cross attends between scene points, action position samples, language tokens and proprioception.

A core part of this algorithm is that it extracts information from the scene through a self-attention operation on the points in the scene and the noisy trajectory candidate. This has several disadvantages. For one this operation is slow, with time complexity growing quadratically with the number of points in the scene. Furthermore, since this step requires an up-to-date diffusion trajectory candidate, it must be performed again for each diffusion iteration, drastically slowing inference. Next, we believe it is a likely cause of 3DDA’s failure to generalize well to unseen camera poses. Because this operation conditions on the 3D geometry of the scene when it self-attends between the points in the scene, it is susceptible to overfitting to that geometry, leading to issues when generalizing to new camera viewpoints.

GenDP [58] is a recent method which extends D³Fields [59] to general manipulation policies. The key idea is to extract DINOv2 [37] features from the images, which are lifted into 3D. It uses the descriptor field algorithm from Wang et al. [59] to combine features from several viewpoints. Then, it computes cosine similarity between these features and some hand-selected task-relevant reference features (such as shoelaces on a shoe) to compute a semantic feature map. It concatenates these features with Cartesian coordinates to form final representations which it processes with a PointNet++ [42] into a final conditioning vector for a diffusion policy.

Beyond some of the point cloud processing details discussed in Sections III-B and III-C, the key difference between GenDP and Adapt3R is GenDP’s dependence on hand-selected reference features in their construction of the semantic feature map. While this may be acceptable in their setting, where they set out to achieve object instance generalization for specific tasks, this is not scalable to a multitask setting, where it would be necessary to define such reference features for each tasks. Adapt3R directly uses the outputs of its RGB backbone without need for task-specific reference features.

B. Extended Method Details

Here we present detailed information about the methods behind the experiments, including detailed information about the inputs to the policies, hyperparameter choices, and action decoder implementation details.

All policies have access to two cameras, as described in Section C. All policies have access to proprioceptive information including end effector position and gripper state. All the baseline methods concatenate it and pass it through an MLP encoder, while Adapt3R uses it to transform the point cloud into the end effector’s coordinate frame.

We use the following hyperparameters for all experiments:

| Parameter | Value |
|-------------------------|-----------------------|
| Optimizer | Adam [23] |
| Learning Rate | 1×10^{-4} |
| Weight Decay | 1×10^{-4} |
| Scheduler | Cosine Annealing [31] |
| Batch Size | 64 |
| Grad Clip | 100 |
| # Train Epochs | 100 |
| Temporal Aggregation | True |
| Embed Dimension d_e | 256 |
| # Downsample Points p | 512 |
| Weight Initialization | Orthogonal [19] |

TABLE VII: Shared hyperparameters across all experiments

1) *Action Decoders*: The **Action Chunking Transformer** [68] (ACT) is a model designed for sequential decision-making tasks, particularly in robotic manipulation. As described in Section III-D, ACT optimizes a variational objective.

In Zhao et al. [68]’s implementation, the RGB input is a sequence of patch embeddings. For our implementation we replace this with the output of either the Adapt3R perception backbone or the backbones described in Section IV-B, which we found to simplify the pipeline and still achieve very strong performance. Additionally, for Zhao et al. [68]’s implementation the VAE encoder only conditions on proprioceptive information, since it would be too inefficient to also condition on all of the perception outputs. Since our version has far fewer tokens to condition on, the encoder conditions on them without efficiency issues.

For the KL weight we found $\beta = 10$ to be good. For baselines we found that a chunk size of $H = 15$ worked well and for Adapt3R we got best results with $H = 10$.

Diffusion Policy [6] is a method which uses DDPMs [18] as a generative model to sample actions from demonstrator action distributions. As discussed in Section IV-B, it does this by learning a reverse Langevin dynamics process using an MSE objective. There are several design choices to make in designing a diffusion policy. We used the CNN UNet version of the model with delta pose actions. For conditioning, we concatenate perception, proprioception and language embeddings, which we project down to d_e and use as global conditioning.

We use the DDIM [52] scheduler with 100 training steps and 10 inference steps and a `squaredcos_cap_v2` beta schedule. For Adapt3R we found a chunk size of $H = 8$ to work well, while a chunk size of $H = 16$ worked well for baselines.

BAKU [15] is a recently released imitation learning algorithm which feeds all inputs into an GPT-style transformer observation trunk, followed by a readout token. The readout token is used as conditioning for an arbitrary action head, and in our case we used an MLP.

With the exception of chunk size, we use the default hyperparameters from Haldar et al. [15]. For chunk size, we use a value of $H = 10$ and $H = 15$ for the baselines and Adapt3R respectively.

C. Experiment Details

In this section we provide further details and visualizations describing the experiments described in Section IV

1) *LIBERO Environment Details*: Most of our experiments use the LIBERO-90 benchmark [29]. The benchmark consists of 90 tasks and corresponding language instructions, and is designed to evaluate agents’ lifelong learning capabilities. The tasks are spread across 20 scenes in 3 settings (Kitchen, Living Room, Study).

For all experiments, the action space is delta poses, and the robots are controlled by the Robosuite OSC controller [69].

For the **change of robot experiment**, we replaced the Franka Panda with the robots shown in Figure 3. Since the robots are controlled by delta pose actions, they share an action space and we could run the outputs from the policy with no further processing. Since we use the gripper joint states as proprioception input, we used the Franka Panda end effector for all robots. In addition to the robots in Figure 3 we tried the Sawyer robot, but found it to have low success rates ($< 15\%$) for all algorithms.

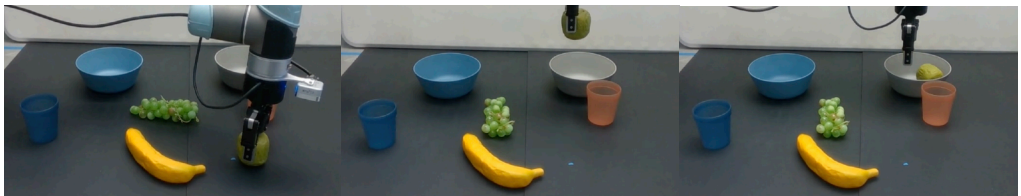
The LIBERO benchmark comes with 50 initialization states for each task, which specify the poses of the robots and all objects in the scene for deterministic evaluation. For the change of robot experiment, we process these such that all objects in the scene have the original pose, and the end effector of the new robot has the same pose as the original end effector. We found that without this change (ie using the end effector’s default initialization pose) all policies had very low success rates, presenting a compelling challenge for future work.

For the **change of camera experiments** we simply moved the camera and updated the camera calibration matrices. Specifically, for the `small` change, we shift the camera by $(0.0, +0.3, -0.1)$ m, for the `medium` change, we shift the camera by $(-0.2, +0.7, -0.2)$ m and for the `large` change, we shift the camera by $(-1.2, +1.0, -0.2)$ m. For all camera position changes we subsequently rotate the camera such that it is facing the end effector’s starting location.

2) *Real Experiment Details*: Our dataset includes a total of 437 trajectories for 6 tasks. In Table VIII we present exact statistics about the datasets for the 6 tasks. In Figure 7 we show visualizations of all tasks present in our multitask imitation learning benchmark.

Our hardware setup is described in detail in Section V-A. For all policies we use end effector pose as proprioceptive input. For all objects we select a home location and initialize them within a 10 cm radius of that home location. For objects which are not axisymmetric about the vertical axis (eg. the banana and grapes) we randomly rotate them. At evaluation time we deterministically initialize object poses in a grid near the home location.

"Pick up the apple and place it in the grey bowl"



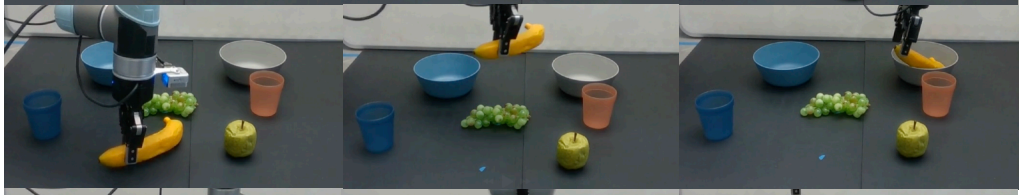
"Pick up the apple and place it in the blue cup"



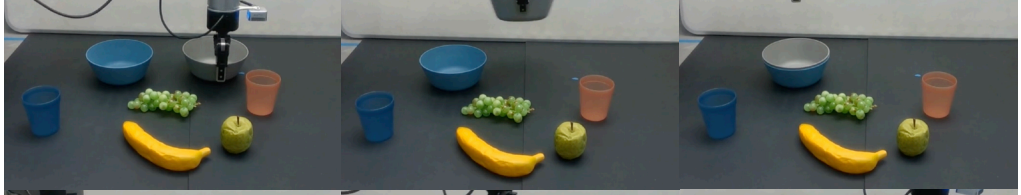
"Pick up the grapes and place them in the blue bowl"



"Pick up the banana and place it in the grey bowl"



"Pick up the grey bowl and stack it in the blue bowl"



"Pick up the blue cup and stack it in the pink cup"



Fig. 7: Our real-world multitask imitation learning benchmark includes 6 pick-and-place tasks shown above.

| Task No. | Language Instruction | # Trajectories | # Samples |
|----------|-------------------------------------------------------|----------------|-----------|
| 1 | “Pick up the apple and place it in the grey bowl” | 87 | 19209 |
| 2 | “Pick up the apple and place it in the blue cup” | 80 | 15925 |
| 3 | “Pick up the grapes and place them in the blue bowl” | 59 | 10339 |
| 4 | “Pick up the banana and place it in the grey bowl” | 74 | 14635 |
| 5 | “Pick up the grey bowl and stack it in the blue bowl” | 60 | 10775 |
| 6 | “Pick up the blue cup and stack it in the pink cup” | 77 | 16583 |
| Total | | 437 | 87466 |

TABLE VIII: Statistics about our real dataset.

D. Further Results and Visualizations

In this section we present additional results that did not fit in the main paper.

1) *Architecture*: In this section we study design choices in the final part of our pipeline, which reduces the point cloud constructed in Section III-B into a single vector for use as conditioning for the action decoder. Overall we conclude that this design choice is not as important as the design choices discussed earlier in the paper.

Our pipeline uses an attention pooling reduction as described in Section III-C. We compare to the following architectures:

- The architecture from **DP3** [66], which runs each point through an MLP before performing max pooling across the point cloud. This method is similar to ours, but replacing the attention pooling with max pooling.
- The architecture form **iDP3** [65], which replaces the MLP in the DP3 architecture with a convolutional pyramid.
- The architecture from **GenDP** [58], which uses PointNet++ [42], a hierarchical point processing architecture.

TABLE IX: How do choices in the embedding extractor architecture affect the final success rate? In this table we present success rates after varying the architecture as discussed in Section D1. While Adapt3R has narrowly better overall performance, the results are inconclusive. All experiments are from combining Adapt3R with BAKU.

| | DP3 | iDP3 | GenDP | Ours |
|---------|--------------|-------|--------------|--------------|
| Orig. | 0.920 | 0.881 | 0.886 | 0.919 |
| UR5e | 0.827 | 0.758 | 0.735 | 0.801 |
| Kinova3 | 0.700 | 0.611 | 0.619 | 0.653 |
| IIWA | 0.695 | 0.660 | 0.697 | 0.718 |
| Small | 0.713 | 0.747 | 0.859 | 0.847 |
| Medium | 0.641 | 0.781 | 0.792 | 0.829 |
| Large | 0.649 | 0.747 | 0.781 | 0.829 |

We present results from this comparison in Table IX. Overall, we see that although Adapt3R narrowly outperforms the comparison architectures, the results do not resoundingly indicate any one architecture is best, although they indicate that the iDP3 architecture does not perform well in this setting. This indicates to us that for future work it may be more fruitful to study changes to the structure of the point cloud itself rather than the final embedding extractor architecture.

One unique attribute from our architecture is the use of attention pooling, which allows us to visualize attention maps and understand which parts of the scene our policy attends to at which times, as we do in Figure 8. We visualize attention maps for several tasks before and after the agent has grasped its target object. Overall, we see that before grasping, Adapt3R dedicates more attention to the target object while after grasping, it dedicated more attention to points in the basket, where it is trying to place the target object. These qualitative results indicate that this method shows promise as a means to direct focus to task relevant points, but empirical results in Table IX suggest that this choice requires further study.

2) *RGB Backbone Choice*: In this section we study the choice of RGB backbone used to define f in Section III-B. In the final version of Adapt3R we use a CLIP [45] backbone with frozen weights, similarly with [20]. However, it is unclear whether pretrained CLIP weights are indeed the best choice. To that end, in Table X we compare CLIP weights with pretrained ResNet weights [16], and ablate the finetuning. We also explore the use of DINOv2 [37] in Table XI, which is known to extract richer local features important for robotic manipulation tasks [58, 59].

First of all, we see no clear difference between performance with CLIP weights and ResNet18 weights. This is surprising, and indicates to us that the model is likely not reasoning deeply about the semantic information in F , but rather is using the feature vectors to look up important points.

Another interesting takeaway from Table X is that finetuning does not help with in-distribution settings but is harmful to out-of-distribution settings, especially when transferring to novel camera viewpoints. One explanation is that finetuning leads the backbone to overfit to the dataset and fail more often for slightly OOD states in in-distribution settings and fail frequently for OOD evaluation settings.

Finally, in Table XI, we explore the potential of DINOv2 [37] as a richer feature extractor. DINOv2 is known for capturing detailed local features, as a result of its self-supervised pretraining task, which emphasizes learning spatially localized



(a) Scene Reference

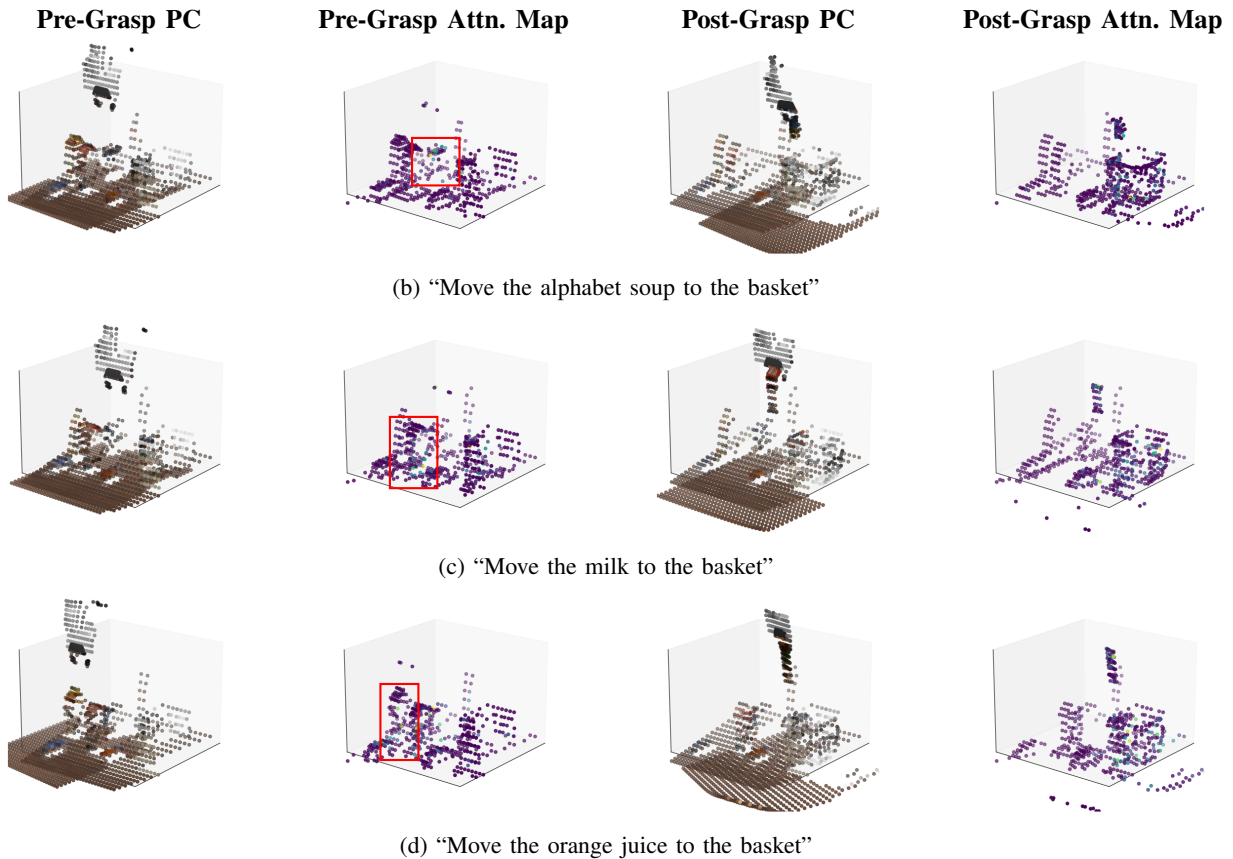


Fig. 8: In this figure we present visualizations of the attention maps at various points during execution for several tasks in the scene shown in (a). Specifically, the tasks are: (b) "Move the alphabet soup to the basket", (c) "Move the milk to the basket", and (d) "Move the orange juice to the basket". For each task we provide (from left to right) a reference point cloud before the end effector has grasped the desired object, the corresponding attention map, a reference point cloud after grasping and while moving towards the basket, and the corresponding point cloud. We also draw a red box around the object the end effector will manipulate to help readers interpret the attention maps. In general we see that while the robot is moving towards the object, it pays more attention to the points corresponding to the object. While moving towards the basket it pays more attention to the basket. We provide videos of these in the "attention maps" folder of the supplementary material.

TABLE X: How does the choice of image feature extractor backbone affect the performance of Adapt3R? ‘FT’ means the model was finetuned while ‘Fr’ means its weights are frozen. ‘RN18’ means a ResNet-18 pretrained with ImageNet weights [16, 7], and CLIP refers to CLIP [45]. All experiments are from the combination of Adapt3R and BAKU.

| | FT RN18 | Fr RN18 | FT CLIP | Fr CLIP |
|---------|---------|--------------|---------|--------------|
| Orig. | 0.909 | 0.906 | 0.912 | 0.919 |
| UR5e | 0.774 | 0.758 | 0.774 | 0.801 |
| Kinova3 | 0.597 | 0.615 | 0.611 | 0.653 |
| IWA | 0.674 | 0.704 | 0.654 | 0.718 |
| Small | 0.840 | 0.848 | 0.819 | 0.847 |
| Medium | 0.819 | 0.840 | 0.806 | 0.829 |
| Large | 0.807 | 0.822 | 0.780 | 0.829 |

representations. This ability could enhance the model’s performance at identifying fine-grained details critical for robotic manipulation tasks. For our experiments, we use the `dinov2_small` model, which outputs a 384-dimensional feature vector for each patch. We modify the stride in the patch extractors and pad the input images to ensure the feature volume output from DINOv2 is compatible with the Adapt3R architecture.

We investigate the usefulness of representations from different layers of DINOv2 by extracting features from various depths:

- **Patch Embeddings:** The embeddings from the patch projection before being passed into the DINOv2 backbone.
- **Layers n :** The feature vectors output by the DINOv2 backbone after being sequentially processed through the first n transformer blocks.

In all cases, we discard the class token (`[CLS]`) to focus on the local features. We avoid experimenting with deeper layers or finetuning as we found DINOv2 feature extraction to be prohibitively time consuming and processing beyond the third layer becomes impractical for both training time and inference speed.

In the original setting, there is no noticeable difference in performance when using DINOv2 features compared to CLIP or ResNet. This consistency across RGB backbones reinforces our earlier claim that the model primarily uses the features to identify task-relevant points rather than leveraging their semantic richness.

In the **change of robot experiments**, DINOv2 features show a slight advantage, with a 2-3% improvement, particularly in the shallowest layer (Layer 1). This may suggest that the local features extracted by DINOv2’s shallow layers are less sensitive to the agent’s embodiment and more focused on the objects and interactions in the scene, enabling better generalization to new robot embodiments.

In the **change of camera experiments** DINOv2 under-performed compared to CLIP or ResNet, likely because the shallow layers in DINOv2 focus on local details and fail to capture the broader spatial context needed for viewpoint changes. CLIP, on the other hand, is better at capturing global information, making it more effective for scenarios involving significant camera shifts. Notably, performance improves when using features from deeper DINOv2 layers, which are known to encode information over larger spatial extents [37]. This highlights the importance of global representations for handling viewpoint changes, as they allow the model to reason about the overall structure of the scene rather than relying solely on local features.

TABLE XI: Effect of using different layers in DINOv2 on the performance of Adapt3R. ‘Patch’ refers to the initial patch embeddings before the DINOv2 backbone, while ‘L1’, ‘L2’, and ‘L3’ denote features extracted after the first, second, and third transformer block, respectively. ‘Ours’ corresponds to the baseline model, Adapt3R using the CLIP backbone with frozen weights. All experiments are from the combination of Adapt3R and BAKU.

| | Patch | L1 | L2 | L3 | Ours |
|---------|-------|--------------|--------------|-------|--------------|
| Orig. | 0.909 | 0.937 | 0.929 | 0.923 | 0.919 |
| UR5e | 0.809 | 0.840 | 0.818 | 0.820 | 0.801 |
| Kinova3 | 0.714 | 0.766 | 0.774 | 0.713 | 0.653 |
| IWA | 0.662 | 0.716 | 0.697 | 0.711 | 0.718 |
| Small | 0.442 | 0.549 | 0.543 | 0.591 | 0.847 |
| Medium | 0.208 | 0.426 | 0.513 | 0.585 | 0.829 |
| Large | 0.167 | 0.437 | 0.558 | 0.654 | 0.829 |

3) *Cropping:* An important detail in several recent works is cropping, or the lack thereof [20, 66, 65]. In this experiment, we set out to understand how different cropping schemes impact the success rate of the final policy. Specifically, we compare the cropping schemes in Figure 9, including:

- No cropping
- Loose cropping, which removes the faraway background but not nearby objects such as the robot base.
- Tight cropping, which removes nearer objects such as the robot base but does not remove the table.

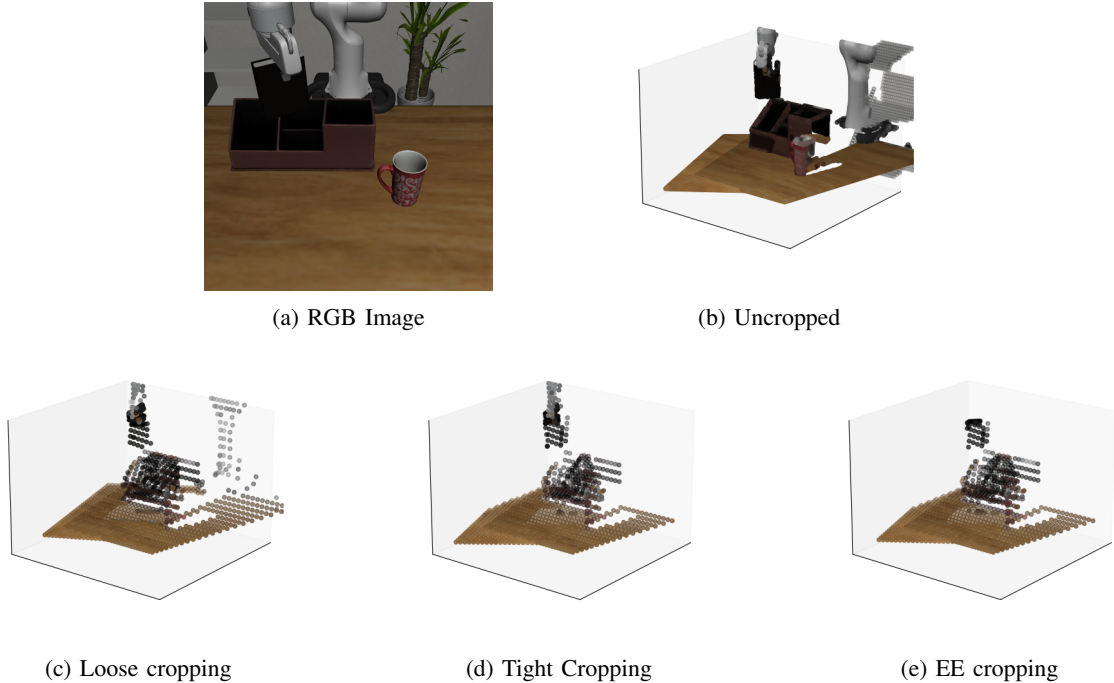


Fig. 9: In this figure we present visualizations of the various cropping schemes discussed earlier in the paper. (a) The original RGB for reference. (b) The uncropped point cloud. The background is visible behind the robot. (c) Loose cropping. The robot is visible but the background is not. (d) Tight cropping. The table is fully visible but the robot base is not. (e) Tight cropping + hand cropping. We use the robot’s proprioception to remove all points behind the end effector.

TABLE XII: The effect of world frame cropping on Adapt3R. ‘None’ means no cropping, ‘Loose’ means that the background is cropped out but objects near the table, such as the robot, are not cropped out (see Figure 9c). ‘Tight’ means that nearer objects such as the robot base are cropped out. ‘No EE’ omits the end effector cropping discussed in Section III-C, and all other experiments use it. All experiments are from combining Adapt3R with BAKU.

| | None | Loose | Tight, No EE | Tight |
|---------|--------------|--------------|--------------|--------------|
| Orig. | 0.917 | 0.914 | 0.913 | 0.919 |
| UR5e | 0.772 | 0.790 | 0.778 | 0.801 |
| Kinova3 | 0.648 | 0.641 | 0.674 | 0.653 |
| IWA | 0.695 | 0.715 | 0.700 | 0.718 |
| Small | 0.858 | 0.849 | 0.834 | 0.847 |
| Medium | 0.830 | 0.830 | 0.822 | 0.829 |
| Large | 0.802 | 0.813 | 0.821 | 0.829 |

- EE cropping, which crops out points behind the end effector.

Results are presented in Table XII. We see that cropping leads to a modest improvement in in-distribution performance. Surprisingly it does not lead to a substantial improvement for the change of robot experiments, with the exception that end effector cropping leads to a modest improvement. We see that cropping does lead to a noticeable improvement for the camera change experiments. This makes sense since these experiments introduce many out of distribution faraway points that are subsequently cropped out.

4) *Downsampling*: In this section we study the downsampling strategies discussed in Section III-C. Specifically, we compare the position-based downsampling used by DP3 [66] and iDP3 [65] to downsampling based on image features in F , as in [20].

First, we compare quantitative results in Table XIII. We see that feature-based downsampling leads to strong improvements across the board, especially when generalizing to novel camera viewpoints. This is likely because changing camera positions introduces a large number of out of distribution points on the table, and downsampling according to features, which removes many repetitive points with the same features corresponding to points on the table, helps to mitigate their influence on the final policy.

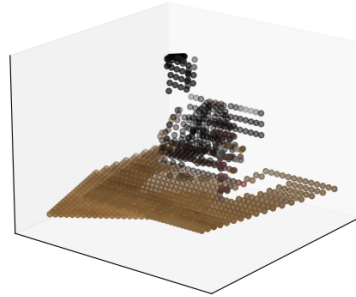
Next, we study a qualitative comparison of the two strategies in Figure 10. We see in Figure 10c that position-based downsampling samples many points on the table, whereas in Figure 10d, the points are concentrated more around the objects

TABLE XIII: How does the choice of metric space for downsampling affect downstream performance? In this table we compare performance with different choices of metric space for farthest point sampling. We see that sampling according to ℓ_2 distance between features in F (right) outperforms sampling based on distances between Cartesian coordinates (left). Based on combining Adapt3R with BAKU.

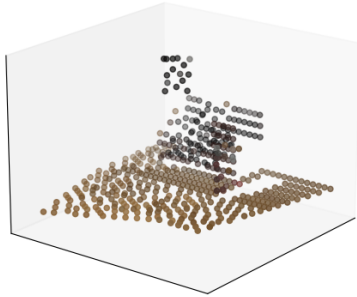
| | Position-Based FPS | Feature-Based FPS |
|---------|--------------------|-------------------|
| Orig. | 0.916 | 0.919 |
| UR5e | 0.768 | 0.801 |
| Kinova3 | 0.596 | 0.653 |
| IIWA | 0.642 | 0.718 |
| Small | 0.717 | 0.847 |
| Medium | 0.651 | 0.829 |
| Large | 0.709 | 0.829 |



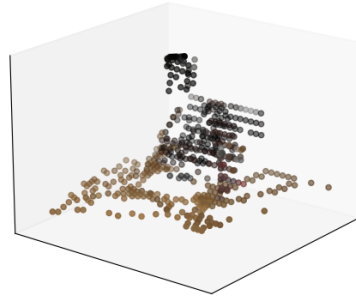
(a) RGB Image



(b) No downsampling



(c) Downsampling based on location



(d) Downsampling based on image features F

Fig. 10: In this figure we present visualizations of the various downsampling schemes discussed earlier in the paper. (a) RGB image of the scene for reference. (b) The original point cloud after cropping. (c) The point cloud after downsampling based on Cartesian coordinates. (d) Downsampling based on image features F .

in the scene.

Finally, we study the effect of p , the hyperparameter controlling the number of points in the downsampled point cloud, in Table XIV. We see that it is not particularly sensitive to this hyperparameter, with a slight improvement for $p = 512$.

5) *Proprioception*: In Table XV we study the effect of proprioceptive inputs on the final LIBERO results. The logic in removing it is that, because the point cloud is in the end effector’s coordinate frame, the proprioceptive information is arguably baked into the observation. We see that removing the proprioception leads to a modest benefit for in-distribution and change of embodiment experiments, but leads to a massive degradation in performance when changing camera poses. Thus, for our final model we include proprioception.

TABLE XIV: In this table we vary the number of points in the downsampled point cloud, p , when combining Adapt3R with BAKU. We see that while performance is not particularly sensitive to this hyperparameter, there is slightly better performance for $p \in \{256, 512\}$.

| | $p = 128$ | $p = 256$ | $p = 512$ | $p = 1024$ |
|---------|-----------|--------------|--------------|------------|
| Orig. | 0.917 | 0.919 | 0.919 | 0.918 |
| UR5e | 0.785 | 0.802 | 0.801 | 0.776 |
| Kinova3 | 0.643 | 0.681 | 0.653 | 0.643 |
| IIWA | 0.725 | 0.745 | 0.718 | 0.672 |
| Small | 0.828 | 0.843 | 0.847 | 0.835 |
| Medium | 0.802 | 0.804 | 0.829 | 0.803 |
| Large | 0.814 | 0.804 | 0.829 | 0.799 |

TABLE XV: with and without proprioception

| Algorithm | Orig. | UR5e | Kinova3 | IIWA | Small | Medium | Large |
|------------------------|--------------|--------------|--------------|--------------|--------------|--------------|--------------|
| ACT + Adapt3R without | 0.916 | 0.824 | 0.796 | 0.760 | 0.671 | 0.472 | 0.452 |
| ACT + Adapt3R with | 0.912 | 0.789 | 0.773 | 0.731 | 0.779 | 0.702 | 0.760 |
| DP + Adapt3R without | 0.899 | 0.761 | 0.568 | 0.522 | 0.568 | 0.419 | 0.398 |
| DP + Adapt3R with | 0.896 | 0.737 | 0.528 | 0.488 | 0.783 | 0.794 | 0.782 |
| BAKU + Adapt3R without | 0.931 | 0.813 | 0.757 | 0.696 | 0.747 | 0.601 | 0.570 |
| BAKU + Adapt3R with | 0.920 | 0.787 | 0.654 | 0.701 | 0.854 | 0.831 | 0.840 |